

Reinforcement Twinning: from digital twins to model-based reinforcement learning

Lorenzo Schena^{a,b}, Pedro Marques^{a,c}, Romain Poletti^{a,d}, Samuel Ahizi^a, Jan Van den Berghe^{a,e}, Miguel A. Mendez^a

^avon Karman Institute, Rhode-St-Genése, 1640, Belgium

^bVrije Universiteit Brussel (VUB), Department of Mechanical Engineering, Elsene, Brussels, 1050, Belgium

^cUniversité Libre de Bruxelles, Av. Franklin Roosevelt 50, Brussels, 1050, Belgium

^dUniversity of Ghent, Sint-Pietersnieuwstraat 41, Ghent, 9000, Belgium

^eInstitute of Mechanics, Materials, and Civil Engineering (iMMC), Université Catholique de Louvain, , Louvain-la-Neuve, 1348, Belgium

Abstract

We propose a novel framework for simultaneously training the digital twin of an engineering system and an associated control agent. The training of the twin combines methods from data assimilation and system identification, while the training of the control agent combines model-based optimal control and model-free reinforcement learning. The combined training of the control agent is achieved by letting it evolve independently along two paths: one driven by a model-based optimal control and another driven by reinforcement learning. The virtual environment offered by the digital twin is used as a playground for confrontation and indirect interaction. This interaction occurs as an “expert demonstrator”, where the best policy is selected for the interaction with the real environment and “cloned” to the other if the independent training stagnates. We refer to this framework as Reinforcement Twinning (RT).

The framework is tested on three vastly different engineering systems and control tasks, namely (1) the control of a wind turbine subject to time-varying wind speed, (2) the trajectory control of flapping-wing micro air vehicles (FWMAVs) subject to wind gusts, and (3) the mitigation of thermal loads in the management of cryogenic storage tanks. The test cases are implemented using simplified models for which the ground truth on the closure law is available. The results show that the adjoint-based training of the digital twin is remarkably sample-efficient and completed within a few iterations. Concerning the control agent training, the results show that the model-based and the model-free control training benefit from the learning experience and the complementary learning approach of each other. The encouraging results open the path towards implementing the RT framework on real systems.

Keywords: Digital Twins, System Identification, Reinforcement Learning, Adjoint-based Assimilation

1. Introduction

Mathematical models of engineering systems have always been fundamental for their design, simulation and control. Recent advances in the Internet of Things (IoT), data analytics and machine learning are promoting the notion of ‘dynamic’ and ‘interactive’ models, i.e. architectures that integrate and enrich the mathematical representation of a system with real-time data, evolve through the system’s life-cycle, and allow for real-time interaction. Such kinds of models are currently referred to as *digital twins*.

Although the specific definition can vary considerably in different fields (Wagner et al., 2019; Barricelli et al., 2019; Chinesta et al., 2020; Rasheed et al., 2019; Ammar et al., 2022; Wright and Davidson, 2020; Tekinerdogan, 2022; van Beek et al., 2023; Haghshenas et al., 2023), a digital twin is generally seen as a virtual replica of a physical object (or system) capable of simulating its characteristic, functionalities and behaviour *in real-time*.

Besides the obvious need for domain-specific knowledge and engineering, constructing such a replica involves various disciplines, from sensor technology and instrumentation for real-time monitoring to virtual/augmented reality and computer graphics for interfacing and visualization, and data-driven modelling, assimilation and machine learning for model updating and control. This work focuses on the last aspects and the required intersection of disciplines, with a particular emphasis on the need for real-time interaction. Real-time predictions are essential to deploying digital twins for control or monitoring purposes and require fast models. Fast models can be built from (1) macroscopic/lumped formulations, eventually enriched by data-driven ‘closure’ laws, (2) surrogate/template models, or (3) reduced-order models derived from high-fidelity simulations. In the context of system identifications for control purposes, the first would be referred to as ‘white’ models; the second would be referred to as ‘black box models’ while the third falls somewhere in between (see Schoukens and Ljung (2019) for the palette of grey shades in data-driven models). Regardless of the approach, the main conceptual difference between digital twinning and traditional engineering modelling is the continuous model update to synchronize the twin with the physical system and to provide a *live* representation of its state from noisy and partial observations.

It is thus evident that the notion of digital twin lies at the intersection between established disciplines such as system identification (see Nelles (2001); Ljung (2008); Nicolao (2003)) and data assimilation (see Asch et al. (2016); Bocquet and Farchi (2023)). Both are significantly enhanced (and perhaps more intertwined) by the rapid growth and popularization of machine learning, as reviewed in the following section of this article. Both seek to combine observational data with a numerical model, and both involve an observation phase (known as training or calibration, depending on the field) in which the model is confronted with online data and a ‘prediction’ phase in which the model is interrogated. However, these disciplines are built around different problems and use different methods.

Data assimilation is mostly concerned with the *state estimation* problem. It is assumed that the model is known (at least within quantifiable uncertainties), but observations are limited and uncertain. These uncertainties are particularly relevant because the system is chaotic and extremely high dimensional (e.g. atmospheric/oceanic models) and thus highly sensitive to the initial conditions from which predictions are requested. The traditional context is weather prediction and climate modelling (Lorenz, 1986; Wang et al., 2000; Pu and Kalnay, 2018; Lahoz et al., 2010), where the goal is to forecast the future evolution of a system from limited observations. The most common techniques are 4D variational assimilation (Talagrand and Courtier, 1987; Dimet et al., 2016; Ahmed et al., 2020) and, more recently, Ensemble Kalman methods (Evensen, 2009; Bocquet, 2011; Routray et al., 2016). Much effort is currently ongoing towards methods that combine these techniques (e.g. Kalnay et al. 2007; Lorenz et al. 2015).

Nonlinear system identification is mostly concerned with the *model identification* problem. The system is subject to external inputs and observed through noisy measurements but is deterministic. The model can be fit into structures that are derived either from first principles or from general templates such as NRAX or Volterra models (Schoukens and Ljung, 2019), and the main goal is to predict how the system responds to actuation. The traditional context is control engineering, i.e. driving the system towards a desired trajectory. Besides the stronger focus on input-output relation (and thus the focus on actuated systems), the main difference with respect to traditional data assimilation is in the deterministic nature of the system to be inferred: errors in the initial conditions are not amplified as dramatically as, for example, in weather forecasting. Therefore, the resulting uncertainties remain within the bounds of model uncertainties. Moreover, in many actuated systems, the forced response dominates over the natural one and the initial conditions are quickly forgotten. Tools for system identification are reviewed by Nelles (2001) and Suykens et al. (1996).

Machine learning is progressively entering both communities with a wealth of general-purpose function approximations such as Artificial Neural Networks (ANNs, see Goodfellow et al. 2016) or Gaussian Processes (GPr, see Rasmussen and Williams 2005). More specifically, the fusion between these disciplines materializes through a combination of variational or ensemble tools from data assimilation to train dynamic models with model structures from machine learning to solve identification, forecasting or control problems. In this regard, the literature in control engineering has significantly anticipated the current developments (see neural controllers in Suykens et al. 1996; Norgaard et al. 2000), although their extension to broader literature has been limited by the mathematical challenges of nonlinear identification and the success of much simpler

strategies based on piece-wise linearization or adaptive controllers (Astrom and Wittenmark, 1994; Sastry and Isidori, 1989).

While machine learning enters the literature of data assimilation and system identification, cross-fertilization proceeds bilaterally. The need for identifying dynamic models from data is also growing in the literature on reinforcement learning, which is significantly drawing ideas from system identification and optimal control theory. Reinforcement learning is a subset of machine learning concerned with the training of an agent via trial and error to achieve a goal while acting on an environment (Sutton and Barto, 2018; Bertsekas, 2019). The framework differs from classic control theory because of its roots in sequential decision making: the environment to be controlled and the agent constitute a Markov Decision Process (MDP, Puterman (1994)) rather than a dynamical system. Model-free approaches solely rely on input-output information and function approximations of the agent’s performance measures, while model-based approaches combine these with a model of the environment (Moerland et al., 2022a; Luo et al., 2022a). The model can be used as a forecasting tool, thus playing the same role as in model predictive control, or as a playground to accelerate the learning (Schwenzer et al., 2021). Model-free approaches have gained burgeoning popularity thanks to their success in video games (Szita, 2012; Mnih et al., 2013a) or natural language processing (Uc-Cetina et al., 2022), for which the definition of a system model is cumbersome. However, these algorithms have shown significant and somewhat surprising limitations for engineering problems governed by simple PDEs (Werner and Peitz, 2023; Pino et al., 2023).

This article proposes a framework combining ideas from data assimilation, system identification and reinforcement learning with the goal of: (1) training a digital twin on real-time data and (2) solving a control problem. We refer to this framework as Reinforcement Twinning (RT). The rest of the article is structured as follows. Section 2 provides a concise literature review of related works across the intersected disciplines and identifies the main novelties of the proposed framework. Section 3 presents the general framework and the key definitions, while Section 4 goes into the mathematical details of its implementation. Section 5 introduces three test cases selected for their relevance in the engineering literature and stemming from largely different fields. These are (1) the control of a wind turbine subject to time-varying wind speed, (2) the trajectory control of flapping-wing micro air vehicles (FWMAVs) subject to wind gusts, and (3) the mitigation of thermal loads in the management of cryogenic storage tanks. Although all test cases are analyzed using synthetic data and are thus somewhat contrived, the main focus is here to show that the model-based and the model-free training can benefit from each other. Section 6 presents the main results; section 7 closes with conclusions and perspectives.

2. Related Work

We briefly review recent developments in methods combining techniques from data assimilation (Section 2.1), system identification (Section 2.2) and model-based reinforcement learning (Section 2.3). We then briefly report on the main novelties of the proposed approach in Section 2.4.

2.1. Machine learning for Data Assimilation

An extensive overview of the state of the art of data assimilation (DA) is provided by Carrassi et al. (2017) while Cheng et al. (2023) give an overview of how machine learning (ML) is entering DA. Geer (2021) discuss the formal links between DA and ML in a Bayesian framework while Abarbanel et al. (2017) analyzes the link by building parallelism between time steps in a DA problem and layer labels in a deep ANN. As explored in Bocquet (2011), the formulation of hybrid DA-ML algorithms consists in introducing ML architectures either (1) to complement/correct the forecasting or the observation model or (2) to replace at least one of them. An early attempt at DA-ML hybridization within the first class was proposed by Tang and Hsieh (2001), who used a variational approach to train an ANN that replaces missing dynamical equations. More recent approaches within the first category are proposed by Arcucci et al. (2021) while Buizza et al. (2022) presents several approaches in both categories. In particular, Arcucci et al. (2021) implements a Recurrent Neural Network (RNN, Madhavan 1993) to correct the forecasting model, while Buizza et al. (2022) use convolutional neural networks (CNNs) to improve the observations passed to a Kalman filter. Within the

second class of hybrid DA-ML methods, Brajard et al. (2020) and Buizza et al. (2022) use a Kalman filter to train the parameters of an ANN that acts as a forecasting model. Outside geophysical sciences, the use of ANNs as a forecasting tool in assimilation frameworks is spreading in economics (Khandelwal et al., 2021) and epidemiology (Nadler et al., 2020). Finally, within the literature on data assimilation, several works have combined ML and DA strategies for model identification (Bocquet et al., 2019; Ayed et al., 2019).

2.2. Machine learning for System Identification and Control

Recent reviews on deep learning for system identifications are proposed by Ljung et al. (2020) and Pillonetto et al. (2023) while earlier reviews are provided by Ljung (2008), Nicolao (2003). System identification has been historically influenced by developments in machine learning and adopted the use of ANNs for system modelling already in the 90’s (Chen et al., 1990; Zhang and Moore, 1991; Sjöberg et al., 1994). Early works (see also Suykens et al. 1996 and Norgaard et al. 2000) focused on the use of feedforward neural networks (FNNs) or recurrent neural networks (RNNs); these can be seen as special variants of nonlinear autoregressive and nonlinear state-space models. The popularization of ML has significantly enlarged the zoology of ANNs architectures used as model structures. The most popular examples include variants of the RNN, such as long-short-term memory (LSTM) networks (Hochreiter and Schmidhuber, 1997) and Echo State Networks (ESN, Jaeger and Haas (2004)), as well as convolutional neural networks (CNNs, LeCun et al. (1989)) and the latest developments in neural ODEs (also known as ODE-net, Chen et al. (2018)).

Important contributions within the first class of approaches are the works by Ljung et al. (2020) and Gonzalez and Yu (2018), who use LSTM networks (Hochreiter and Schmidhuber, 1997). These are variants of RNNs, which are very popular in natural language processing and use three gates (forget/input/output) to preserve information over longer time steps, thus allowing for better handling of long-term dependencies. Canaday et al. (2020) used ESNs, which gained popularity for forecasting in stochastic systems. These are variants of RNNs implementing the reservoir computing formalism, i.e. ANNs in which weights and biases are selected randomly. Andersson et al. (2019) used CNNs, which gained popularity in image recognition and allow for identifying patterns at different scales, while Ayed et al. (2019); Rahman et al. (2022) use ODE-nets, recently proposed as a new paradigm for neural state-space modelling. ODE-nets treat the layers of an ANN as intermediate time steps of a multistep ODE solver and are commonly trained using the adjoint method, a ubiquitous tool in data assimilation.

2.3. Model Based Reinforcement Learning and Optimal Control

Recent reviews of model-based reinforcement learning (MBRL) are proposed by Chatzilygeroudis et al. (2019), Luo et al. (2022b) and Moerland et al. (2022b). MBRL uses a model of the environment to guide the agent, with the goal of increasing its sample efficiency (i.e. reducing the number of trials required to learn a task). A model allows the agent to sample the environment with arbitrary state-action values. In contrast, a model-free approach can only sample visited states, eventually stored in a replay buffer to allow multiple re-uses (Haarnoja et al., 2018; Lillicrap et al., 2019). In the reinforcement learning terminology, a model allows the agent to *plan*, giving the possibility to *imagine* the consequences of actions and, more generally, update policy and/or state-action value predictors without interacting with the environment.

MBRL methods can be classified based on how the model is built and how it is used. Concerning the approaches for model constructions, a large arsenal of function approximations has been deployed in the literature. ANNs (Hunt et al., 1992; Kurutach et al., 2018; Nagabandi et al., 2017), Gaussian Processes (GPr (Deisenroth and Rasmussen, 2011; Boedecker et al., 2014a)) and time-varying linear models (Boedecker et al., 2014b) are some examples. Concerning model usage, the simplest approach consists of using it solely to sample the state-action space, while more advanced approaches use the model in the training steps. One of the seminal MBRL approaches is the Dyna algorithm proposed by Sutton (1991). This uses experience (i.e. trajectories in the state-action space and associated rewards) collected from both environment and model. More sophisticated approaches use the model to “look ahead”, i.e. predicting the future evolution of the system under a given policy. A notable example is the Monte Carlo Tree Search in the AlphaGO (Silver et al., 2016, 2018) algorithm that reached superhuman performances in the game of Go. Moving from Markov Decision Processes to dynamical systems, the boundaries between MBRL and Model Predictive

Control (MPC) become blurred, particularly when the latter uses black-box models (see Hedengren et al. 2014; Raw 2000 and Nagabandi et al. 2017 or Weber et al. 2017).

Several authors have proposed methods to leverage physical insights in the models for MBRL, using physics-informed neural networks (Raissi et al., 2019) as Liu and Wang (2021) or Deep Lagrangian Networks (DeLaN Lutter et al. 2019) as Ramesh and Ravindran (2023). A more extreme approach is proposed by Lutter et al. (2020), who uses ‘white-box’ models (eventually enhanced as proposed by Lutter et al. 2020) in MBRL. This work shows a traditional physics-based model trained via machine learning methods. The opposite case is provided by Liu and MacArt (2023), who uses an ANN agent trained with adjoint-based optimization. An overview of methods to integrate physics-based models and machine learning is provided by Baker et al. (2019) and Willard et al. (2020). Regardless of its structure, a differentiable model of the environment can be trained using optimal control theory (Stengel, 1994).

2.4. Novelty of the proposed approach

The RT framework proposed in this work is, in essence, MBRL with a white box (physics-based) model trained with methods from data assimilation. This model allows for real-time interaction and can be seen as a digital twin because it is trained, in real-time, to reproduce the performance of a specific system. Concerning the training, we use an ensemble adjoint-based approach to compute the gradient of the cost function driving the model derivation. This gives remarkable robustness to noise. Variants of the algorithm using Ensemble Kalman filtering are currently being explored.

However, contrary to traditional data assimilation, we assume that all states are observable and the underlying dynamic is deterministic. Moreover, since the main role of the model is to provide input-output relations in an actuated system, the approach is closer to system identification than traditional data assimilation. Finally, contrary to MPC, we assume that not all inputs to the system can be predicted; hence, the model cannot ‘look ahead’. However, the ensemble approach to handle the unpredictable inputs allows for online planning. Extensions to an MPC formalism are left to future work.

3. Definitions and General Formulation

The main components of the RT approach implemented in this work are illustrated with the aid of the schematic in Figure 1. All components are numbered following the presentation below.

We consider a dynamical system (component 1) with states $\tilde{\mathbf{s}} \in \mathbb{R}^{n_s}$ evolving according to *unknown* dynamics. We treat this system as a black box and consider it the *real* environment. We assume that these states can be sampled (measured) at uniform time intervals $t_k = k\Delta t$ over an observation time T_o to collect the sequence $\tilde{S} = [\tilde{\mathbf{s}}_1, \dots, \tilde{\mathbf{s}}_{n_t}]$ with $n_t = T_o/\Delta t + 1$. All variables are sampled in the same way, and we use subscripts to identify the sample at specific time steps.

The real system evolves under the influence of control actions $\tilde{\mathbf{a}}_k$, provided by an agent, and exogenous (uncontrollable) inputs $\tilde{\mathbf{z}}_k = \tilde{\mathbf{d}}_k + \tilde{\boldsymbol{\epsilon}}_k \in \mathbb{R}^{n_z}$. We assume that these consist of a ‘large’ scale ($\tilde{\mathbf{d}}_k$) and a ‘small scale’ ($\tilde{\boldsymbol{\epsilon}}_k$) contribution, but neither of the two can be forecasted. These are treated as random processes with different integral time scales. With no loss of generality, we assume that observations and actions occur simultaneously. Therefore, in the reinforcement learning terminology, the collection of n_t observations/action pairs within the observation time T_o defines an *episode*.

The actions seek to keep the system along a desired trajectory $\tilde{S} = [\tilde{\mathbf{s}}_1, \dots, \tilde{\mathbf{s}}_{n_t}]$ (component 2) and we introduce the *real error* $\tilde{\boldsymbol{\epsilon}}_k = \tilde{\boldsymbol{\epsilon}}(\tilde{\mathbf{s}}_k, \tilde{\mathbf{s}}_k) \in \mathbb{R}^{n_s}$ to measure the discrepancy between the current and the target states. The control agent (component 3) acts according to a *policy* which takes the form of a parametric function $\tilde{\mathbf{a}}_k = \pi(\tilde{\boldsymbol{\epsilon}}_k; \mathbf{w}_a)$ in the weights $\mathbf{w}_a \in \mathbb{R}^{n_\pi}$. The control problem involves identifying the weights \mathbf{w}_a through an iterative “learning process” while the agent interacts with the system. This process is carried out by evolving two policies in parallel: the best one is promoted to “live” policy and interacts with the real system while the other becomes “idle” and continues to be trained in the background.

One of these policies evolves according to model-free strategy. It is denoted as π_{mf} and is defined by the set of parameters $\mathbf{w}_{a,mf}$. The other evolves according to a model-based strategy. It is denoted as π_{mb} and is defined by the set of parameters $\mathbf{w}_{a,mb}$. The decision of which of these becomes “live” or “idle” is taken

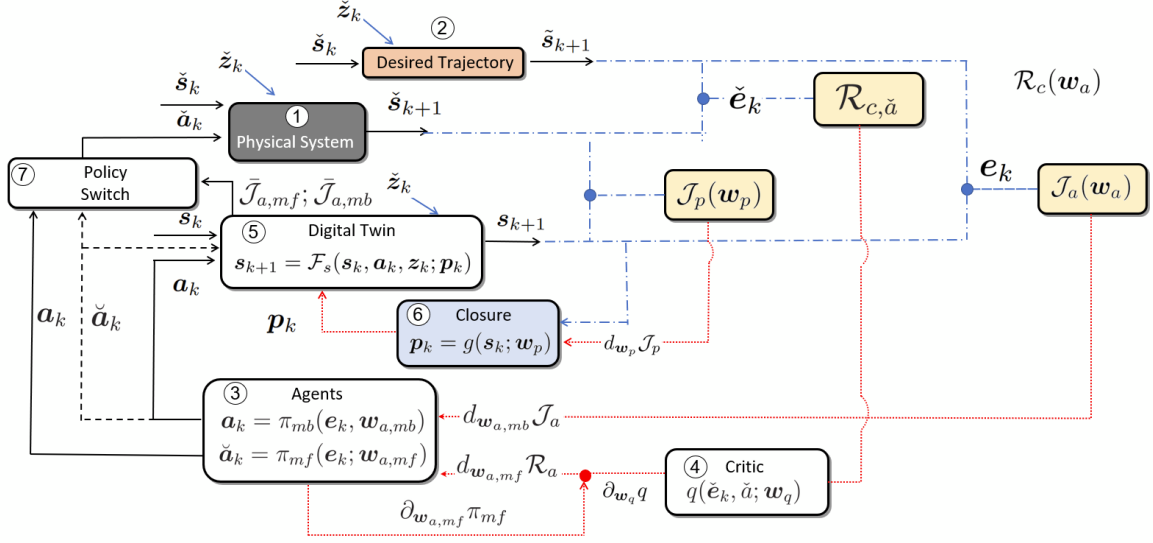


Figure 1: Structure of the proposed approach to blend assimilation, model-based and model-free control. We use one control agent, acting on the physical system and its digital twin, and we combine the learning from a model-free and a model-based approach. The dashed blue lines are used to track the distance measures, while the red dotted lines track the updates of the parameters involved in the training. The full algorithmic implementation is provided in Algorithm 1.1.

by policy switch (element 7 in Figure 1) that selects either $\mathbf{w}_a = \mathbf{w}_{a,mf}$ or $\mathbf{w}_a = \mathbf{w}_{a,mb}$ depending on which of the two is producing the best results on the virtual environment and the digital twin (component 5).

The working principle of this policy switch is described in section 4.3. What follows is a description of the model-free and the model-based training, treated as independent strategies.

- The model-free policy (π_{mf}) training relies on classic model-free reinforcement learning. The optimal weights $\mathbf{w}_{a,mf}$ are defined according to a reward function, which measures how well the system is kept close to the desired trajectory. This evaluation is made *online*, updating the policy after each episode. The optimal weights maximize this function, which is written as the summation of instantaneous rewards $r_k = r(\check{\mathbf{e}}_k, \check{\mathbf{a}}_k) \in \mathbb{R}$, discounted by a factor γ :

$$\mathcal{R}_c(\mathbf{a}) = \sum_{k=0}^{n_t-1} \gamma^k r_k(\check{\mathbf{e}}_k, \check{\mathbf{a}}_k). \quad (1)$$

The definition of the instantaneous reward function is problem-dependent and discussed in the following sections. As described in section 4.1, the model-free loop implemented in this work is an actor-critic algorithm, which relies on a parametric approximation of the state-action value function $Q(\check{\mathbf{e}}, \check{\mathbf{a}}; \mathbf{w}_q)$ in the parameters \mathbf{w}_q . This estimates the expected reward for an action-state pair and is essential in computing the update of the policy parameters \mathbf{w}_a . This parametric function is referred to as ‘critic’ (component 4) and is essential in computing the gradient $d_{\mathbf{w}_{a,mf}} \mathcal{R}_c$ driving the training of the agent from the model-free side (see connections in dashed red in Figure 1). We highlight that the use of the error state \mathbf{e} rather than the state \mathbf{s} in the reward and Q functions is here justified by our focus on tracking problems.

- The model-based policy (π_{mb}) optimization loop combines system identification and optimal control. System identification seeks to continuously adapt and improve the digital twin (component 5). This is a model of the system which evolves the ‘virtual states’ \mathbf{s}_k to \mathbf{s}_{k+1} , subject to the same exogenous inputs $\check{\mathbf{z}}_k$ as the physical system and under the ‘virtual actions’ \mathbf{a}_k . This solver advances the digital twin in real time and restarts at the end of each episode.

The model relies on unknown parameters $\mathbf{p}_k \in \mathbb{R}^{n_p}$, provided by a closure parametric function $\mathbf{p}_k = g(\mathbf{s}_k; \mathbf{w}_p)$ (component 6) in the weights $\mathbf{w}_p \in \mathbb{R}^{n_g}$. This closure function embeds unknown physics or terms that would render the prediction overly expensive. As we shall see in Section 5, these parameters can be classic empirical coefficients (e.g. aerodynamic coefficients or heat/mass transfer coefficients) of a carefully crafted physics-based model of the system. The forward step of the system is driven by an ODE solver, which defines the function $\mathbf{s}_{k+1} = \mathcal{F}_s(\mathbf{s}_k, \mathbf{a}_k, \mathbf{z}_k; \mathbf{p}_k)$.

The system identification consists in finding the optimal weights \mathbf{w}_p according to a cost function $\mathcal{J}_p(\mathbf{w}_p)$ which measures how close the virtual trajectory $S = [\mathbf{s}_1, \dots, \mathbf{s}_{n_t}]$ resembles the real one. The optimal weights \mathbf{w}_p minimize this function, defined as

$$\mathcal{J}_p(\mathbf{w}_p) = \mathbb{E}_{\sim S(\mathbf{z}, \mathbf{w}_p)} \left\{ \int_0^{T_o} \mathcal{L}_p(\tilde{\mathbf{s}}(t_k), \mathbf{s}(t; \mathbf{w}_p)) dt \right\}, \quad (2)$$

with $\mathcal{L}_p : \mathbb{R}^{n_s \times n_s} \rightarrow \mathbb{R}$ the Lagrangian function for the identification problem and the expectation $\mathbb{E}_{\sim S(\mathbf{z}, \mathbf{w}_p)} \{ \}$ over possible virtual trajectories accounting for the stochastic exogenous inputs. More specifically, starting from one sample signal \mathbf{z}_k , with $k = [0, n_t - 1]$, we build a set of N_z realizations of exogenous inputs as described in section 4.2 and we denote as $S(\mathbf{z}, \mathbf{w}_p)$ the set of trajectories generated for a given sample of the exogenous input \mathbf{z} and a given set of weights \mathbf{w}_p . Two reasons motivate the choice for the integral formulation in (2) even if only a discrete set of samples $\tilde{\mathbf{s}}(t_k)$ is available. First, the integral is particularly handy in deriving the adjoint problem driving the computation of the gradient $d_p \mathcal{J}$, as presented in section 4.2. Second, the choice keeps the approach independent from the specific numerical solver to advance the virtual states $\mathbf{s}(t)$. We return to both points in section 4.3. We here stress that the closure model $g(\mathbf{s}; \mathbf{w}_g)$ makes the digital twin predictive only for a given sample of the exogenous disturbance signal and within $t \in [0, T_o]$, i.e. no forecasting is considered.

The model-based control seeks to find the optimal policy to keep the digital twin along the desired trajectory. We introduce the *virtual error* $e(t_k) = e(\mathbf{s}_k, \tilde{\mathbf{s}}_k)$ to measure the distance between the current virtual state and the target state and $\mathbf{w}_{a,mb} = \pi_{mb}(e; \mathbf{w}_{a,mb})$ the *virtual actions* taken on the digital twin. The performances of the controller are measured by the cost function $\mathcal{J}_a(\mathbf{w}_{a,mb})$. For convenience, we define this cost function similarly to the one in (2), i.e.:

$$\mathcal{J}_a(\mathbf{w}_{a,mb}) = \mathbb{E}_{\sim S(\mathbf{z}, \mathbf{w}_{a,mb})} \left\{ \int_0^{T_o} \mathcal{L}_a(\tilde{\mathbf{s}}(t), \mathbf{s}(t; \mathbf{w}_{a,mb})) dt \right\}, \quad (3)$$

with $\mathcal{L}_a : \mathbb{R}^{n_s} \rightarrow \mathbb{R}$ the Lagrangian function for the model-based control problem. The same notation as in (2) applies. The optimal control weights for the model-based approach are those that minimize this function. The process of computing a policy update using the virtual environment (model-based loop) without interacting with the real system is here referred to as *offline (policy) planning*.

It is worth stressing that the weights $\mathbf{w}_{a,mb}$ minimizing \mathcal{J}_a in (3) do not necessarily maximize \mathcal{R}_c in (1). These problems will not have the same solution unless the virtual environment closely follows the real one. The way these loops interact in the agent's training is described in the following section, along with more details on the computation of the gradient $d\mathcal{J}_p/d\mathbf{w}_p$ driving the identification and the gradient $d\mathcal{J}_a/d\mathbf{w}_{a,mb}$ driving the agent's training from the model-based side (see connections in dashed red in Figure 1).

4. Mathematical Tools and Algorithms

We here detail the building blocks of the proposed approach. Only the general architecture is discussed, leaving customizations to specific environments to Section 5. The model-free paradigm (connection of components 1-2-3-4) is illustrated in section 4.1. This leverages standard Deep Reinforcement Learning (DRL) methodologies. The model-based paradigm (connections of components 1-2-3-5-6) is illustrated in section 4.2. This combines adjoint-based nonlinear system identification and adjoint-based optimal control.

The model-free and model-based loops could be used independently, and we first introduce their working principle independently. Then, section 4.3 details how these are connected and presents the proposed algorithm.

4.1. The Model-Free loop: (1)-(2)-(3)-(4)

We consider a classic actor-critic reinforcement learning formalism (Sutton and Barto 2018, Bhatnagar et al. 2009). Although more recent variants exist, we here focus on the classic Deep Deterministic Policy Gradient (DDPG) algorithm proposed by Lillicrap et al. (2019) with the prioritized experience replay strategy by Schaul et al. (2015). This algorithm was extensively benchmarked by Pino et al. (2023) in flow control problems and offers a good compromise between performance and simplicity.

The DDPG trains two ANNs while interacting with the system. The first, referred to as *actor*, aims to approximate the policy function $\pi_{mf} : \check{\mathbf{e}} \rightarrow \check{\mathbf{a}}$, which provides the action to be taken at a certain state. This policy is deterministic, but we add noise generated by a random process to explore action space.

The second, referred to as *critic*, aims to approximate the state action value function $q : (\check{\mathbf{e}}, \check{\mathbf{a}}) \rightarrow Q$; this provides the expected reward for taking action $\check{\mathbf{a}}$ while the system is in the error state $\check{\mathbf{e}}$ and then following a certain policy. We use Q to denote the (unknown) true Q value and $q(\check{\mathbf{e}}, \check{\mathbf{a}}; \mathbf{w}_q)$ to denote the approximation from the Q -network. Referring to the previous section and Figure 1, the parameters \mathbf{w}_a denote the weights and biases of the actor-network while \mathbf{w}_q denotes the weights and biases for the critic network.

These are identified through an online optimization process, which is based on stochastic, momentum-accelerated gradient-based optimization as in classic deep learning (see Goodfellow et al. (2016)). The gradient driving the optimization of the policy reads (see Silver et al. (2014)).

$$\frac{d\mathcal{R}_c}{d\mathbf{w}_a} = \mathbb{E}_{\sim \check{S}} \left\{ \frac{dq(\check{\mathbf{e}}, \check{\mathbf{a}}; \mathbf{w}_q)}{d\mathbf{a}} \frac{d\pi(\check{\mathbf{e}}; \mathbf{w}_a)}{d\mathbf{w}_a} \right\}, \quad (4)$$

where \mathcal{R}_c is the reward function in (1).

The expectation is evaluated on an ensemble of trajectories or transitions and is readily available using back-propagation on the actor and the critic networks. Its accuracy strongly relies on the accuracy of the critic network. The recursive nature of the state value action function allows for measuring the performances of the critic from the Bellman equation (Sutton and Barto, 2018). For the true Q function this reads:

$$Q(\check{\mathbf{e}}_k, \check{\mathbf{a}}_k) = \mathbb{E}_{\sim \mathbf{s}_{k+1}} \left\{ r_k + \gamma Q(\check{\mathbf{e}}_{k+1}, \mathbf{a}_{k+1}^\pi) \right\}. \quad (5)$$

where $r_k = r(\check{\mathbf{e}}_k, \check{\mathbf{a}}_k)$. The expectation over possible future states accounts for the stochastic nature of the exogenous inputs, and \mathbf{a}^π denote actions according to the current policy π (i.e. $\check{\mathbf{a}}_k^\pi = \pi(\check{\mathbf{e}}_k; \mathbf{w}_a)$). The same recursive form should then exist for the q network. Therefore, defining

$$y_k = r_k + \gamma q(\check{\mathbf{e}}_{k+1}, \pi(\check{\mathbf{e}}_{k+1}); \mathbf{w}_q) \quad (6)$$

the expected state-action value at step k , and as $\delta_k = y_k - q(\check{\mathbf{e}}_k, \check{\mathbf{a}}_k)$ the Temporal Difference (TD) error, a cost function for training the critic network can be written as

$$\mathcal{J}_q(\mathbf{w}_q) = \mathbb{E}_{\sim \mathbf{s}_k, \mathbf{s}_{k+1}} \{ \delta_k^2 \}, \quad (7)$$

where the expectation $\mathbb{E}_{\sim \mathbf{s}_k, \mathbf{s}_{k+1}}$ is computed over a set of transitions from one state to the following (regardless of their position in the system trajectory).

The gradient of (7) with respect to \mathbf{w}_q can be easily computed using back-propagation on the critic network. However, the training of the critic network is notoriously unstable (Mnih et al., 2013b, 2015). The two classic approaches to stabilize the learning consist in (1) using an under-relaxation in the update of the weights and (2) keeping track of a large number of transitions by using a replay buffer. The use of both methods is discussed in Section 4.3.

Finally, the sampling from the buffer is carried out in the form of batches to evaluate the gradient $d\mathcal{J}_q/d\mathbf{w}_q$. The sampling prioritizes transitions with the largest TD-error, δ_k , (Schaul et al., 2016) building a

non-zero probability distribution for each sample proportional to it $p_i = |\delta_i| + \text{tol}$, yielding to the sampling probability of the i -th transition, $P(i)$ equal to:

$$P(i) = \frac{p_i^{\alpha^*}}{\sum_k p_k^{\alpha^*}}, \quad (8)$$

in which α^* sets the prioritization influence, with $\alpha^* = 0$ implying uniform sampling.

4.2. The Model-Based Loop (1)-(2)-(3)-(5)-(6)

The assimilation and model-based control problem in the loop (1)-(2)-(3)-(5)-(6) share the same mathematical framework. The dynamical system describing the evolution of the digital twin is written as

$$\begin{cases} \dot{\mathbf{s}} &= f(\mathbf{s}, \mathbf{a}, \mathbf{z}, \mathbf{p}) \\ \mathbf{s}(0) &= \mathbf{s}_0 \\ \mathbf{a} &= \pi_{mb}(\mathbf{e}, \mathbf{w}_{a,mb}); \mathbf{p} = g(\mathbf{s}, \mathbf{w}_p) \end{cases}, \quad (9)$$

where $f : \mathbb{R}^{n_s \times n_a \times n_p \times n_z} \rightarrow \mathbb{R}^{n_s}$ is the flow map of the dynamical system and is here assumed to be known.

This function could be derived from first principles, as described in section 5 for the selected test cases, or using a general-purpose function approximator such as ANNs. The distinction is irrelevant to the method presented in this section, and we note in passing that using an ANN to approximate f in combination with the training techniques described in this section leads to neural ODEs (Chen et al., 2018).

The problem of *training* the agent and the closure law is finding the optimal parameters \mathbf{w}_a and \mathbf{w}_p , respectively, using continuously provided data. The training data consists of a target trajectory $\tilde{\mathbf{s}}(t)$ for the control problem and measurements of the states $\check{\mathbf{s}}(t)$ for the identification problem. The performances of the assimilating agent are measured according to (2) and (3), respectively (see Figure 1).

These functions are interconnected because they depend on the states, which depend on both the closure variables and the actions (thus both on \mathbf{w}_a and \mathbf{w}_p). However, we here consider these independently: \mathbf{w}_p should be identified to minimize \mathcal{J}_p regardless of the performance of the controlling agent, and \mathbf{w}_a should be identified to minimize \mathcal{J}_a regardless of the performances of the assimilating agent. This is why only the relevant functional dependency is considered in equations (2) and (3).

To maximize the sample-efficiency training strategy, the optimization of these functions is carried out using gradient-based optimization along with efficient computation of the gradients $d\mathcal{J}_p/d\mathbf{w}_p$ and $d\mathcal{J}_a/d\mathbf{w}_a$ using the adjoint method (Errico, 1997; Bradley, 2019; Cao et al., 2003). This method bypasses the need for computing the sensitivities $d\mathbf{s}/d\mathbf{p}$ and $d\mathbf{s}/d\mathbf{a}$. Moreover, because of the similarity in the cost functions (2) and (3), the adjoint problems share key terms. Concerning the gradient driving the system identification, the adjoint-based evaluation gives

$$\frac{d\mathcal{J}_p}{d\mathbf{p}} = \mathbb{E}_{\sim S(\mathbf{z}, \mathbf{w}_p)} \left\{ \int_0^{T_o} \boldsymbol{\lambda}_p^T(t) \frac{df}{d\mathbf{p}} \frac{dg}{d\mathbf{w}_p} dt \right\}, \quad (10)$$

where the expectation operator is the same used for the cost function definition in (3), the gradient $dg/d\mathbf{w}_p$ is readily available from the closure definition and $\boldsymbol{\lambda}_p \in \mathbb{R}^{n_s}$ is the vector of Lagrange multipliers (co-states) computed from the terminal value problem:

$$\begin{cases} \dot{\boldsymbol{\lambda}}_p &= - \left(\frac{df}{d\mathbf{s}} \right)^T \boldsymbol{\lambda}_p - \left(\frac{d\mathcal{L}_p}{d\mathbf{s}} \right)^T \\ \boldsymbol{\lambda}_p(T_o) &= \mathbf{0}. \end{cases} \quad (11)$$

Similarly, the computation of the gradient $d\mathcal{J}_a/d\mathbf{p}$ driving the training of the controlling agent is:

$$\frac{d\mathcal{J}_a}{d\mathbf{a}} = \mathbb{E}_{\sim S(\mathbf{z}, \mathbf{w}_a)} \left\{ \int_0^{T_o} \boldsymbol{\lambda}_a^T(t) \frac{df}{d\mathbf{a}} \frac{d\pi}{d\mathbf{w}_a} dt \right\}, \quad (12)$$

where the gradient $d\pi/d\mathbf{w}_a$ is available from the policy definition (e.g. via backpropagation if this is an ANN) and the evolution of the Lagrange multiplier $\boldsymbol{\lambda}_a(t) \in \mathbb{R}^{n_s}$ is determined by the terminal problem:

$$\begin{cases} \dot{\boldsymbol{\lambda}}_a &= -\left(\frac{d\mathcal{L}}{d\mathbf{s}}\right)^T \boldsymbol{\lambda}_a - \left(\frac{d\mathcal{L}_a}{d\mathbf{s}}\right)^T \\ \boldsymbol{\lambda}_a(T_o) &= \mathbf{0}. \end{cases} \quad (13)$$

In both problems, one has one adjoint state evolution $\boldsymbol{\lambda}_p(t)$ and $\boldsymbol{\lambda}_a(t)$ for each of the N_z trajectories used to evaluate the expectation in (10). The methodology to compute the population of trajectories is described in the remainder of this section.

Given a sample of the temporal evolution of the exogenous inputs $\mathbf{z}_k = \mathbf{z}(t_k)$, with $k = [0, n_t - 1]$, we build an analytic approximation of its large-scale component $\mathbf{d}_k = \mathbf{d}(t_k)$ using support vector regression (Smola and Schölkopf, 2004). Let $\mathbf{d}_k[j] \in \mathbb{R}$ denote the j -th component of the exogenous input sampled at time step k . We seek to derive a continuous function $\tilde{\mathbf{d}}[j](t)$ such that $\tilde{\mathbf{d}}[j](t_k) \approx \mathbf{d}_k[j]$. This is a regression problem that we tackle with support vector regression. Hence, the continuous function is written as

$$\tilde{\mathbf{d}}[j](t; \boldsymbol{\alpha}[j]) = \sum_{k=0}^{n_t-1} \alpha[j]_k \kappa(t_k, t) \quad (14)$$

with $t \in \mathbb{R}$, $\kappa(t_1, t_2) = \exp(-\gamma \|t_1 - t_2\|_2^2)$ a Gaussian kernel and γ a user defined scale parameter. We stress that $t \in [0, T_o]$ since no forecasting attempt is made. The vector of coefficients $\boldsymbol{\alpha}[j] = [\alpha[j]_1, \dots, \alpha[j]_{n_t}]$ is computed by minimizing the cost function (see Chang and Lin 2011)

$$J(\boldsymbol{\alpha}[j]) = \frac{1}{2} \|\boldsymbol{\alpha}[j]\|_2^2 + C \left(\sum_{k=0}^{n_t-1} \varepsilon_j + \varepsilon_j^* \right), \quad (15)$$

subject to $\mathbf{z}[j](t_k) - \tilde{\mathbf{d}}[j](t_k, \boldsymbol{\alpha}) < \epsilon + \varepsilon_j$, $\mathbf{z}[j](t_k) - \tilde{\mathbf{d}}[j](t_k, \boldsymbol{\alpha}) > \epsilon + \varepsilon_j$ and $\varepsilon_j \varepsilon_j^* > 0$ for all j in $[1, n_t]$. The coefficients C and ϵ are user-defined parameters controlling the regularization of the regression.

The regression model generates N_z samples of possible exogenous disturbances. These are modelled as a set of n_z Gaussian processes with mean $\tilde{\mathbf{d}}[j](t; \boldsymbol{\alpha}[j])$ and covariance matrices $\boldsymbol{\Sigma}_\varepsilon[j]$. We sample these processes N_z times to obtain the exogenous disturbances in the virtual trajectories. This procedure is shown in Fig. 2, for a simulated exogenous disturbance with $N_z = 10$.

4.3. The proposed RT algorithm

The proposed algorithm is illustrated in 1.1. It consists of six steps, repeated over n_e episodes. These are described in the following.

- **Step 1: Interaction with the real environment (lines 7-13).** A sequence of n_t interactions with the real system takes place within an observation time T_o . These episodes are denoted as *real* as opposed to the *virtual* ones carried out on the digital twin. These interactions may have an exploratory phase, carried out by adding a random component (\mathbf{n}_k) sampled from a random process. We here use a Gaussian process with mean $\boldsymbol{\mu}_a$ and covariance matrix $\boldsymbol{\Sigma}_a$ (line 6). The balance between exploration and exploitation is controlled by the sequence $\xi(i)$, which tends to zero as exploration ends. This sequence could be linked to the performance of the digital twin assimilation, but we leave it as a user-defined sequence for the purposes of this work. During this phase, transitions are stored in the long-term memory buffer \mathcal{D}_L and the short-term memory buffer \mathcal{D}_S . The first is used to update the critic network and the model-free policy and contains transitions ranked by their TD error δ_k (see eq. 7), which is updated as the training of the critic progresses. The second is used for training the digital twin and contains transitions ordered in time and arranged in trajectories. Therefore, \mathcal{D}_L contains n_L (random) transitions while \mathcal{D}_S collects n_S trajectories. The TD error defines both the sampling and the cleaning of the \mathcal{D}_L buffer. The triangular distribution in (8) is used both for sampling and cleaning: the transitions with the lowest probability of being sampled are also the ones continuously replaced

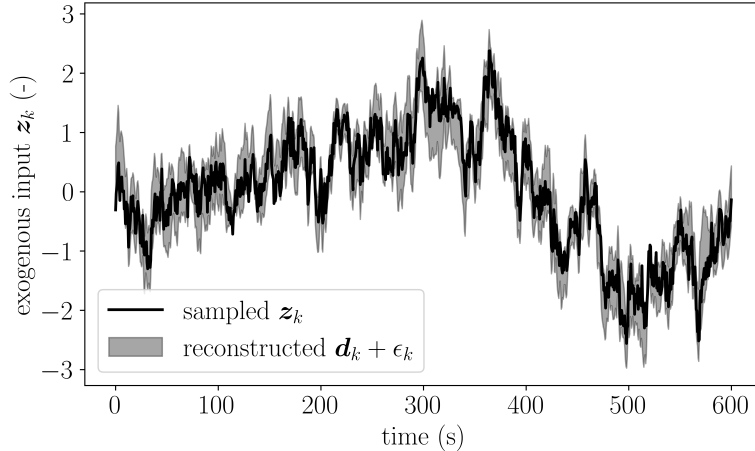


Figure 2: Example of SVR regression of sampled exogenous input. A filtered exogenous input is passed as an input of the SVR (continuous line) which outputs $N_z = 10$ possible realizations.

by the new ones. On the other hand, no specific criteria are considered for the sampling/cleaning of the buffer \mathcal{D}_S , which are simply sampled and stored in chronological order.

- Step 2: Critic Update and model-free policy update (lines 14-24).** An optimization with n_Q iterations is carried out on the critic network, followed by an optimization with n_A iterations for the policy. Both use batches of n_b transitions sampled from \mathcal{D}_L . Concerning the training of the critic network (lines 14-19), this loss function and its gradient are computed from (7). This step is essentially a training of the critic network in a supervised learning formalism. Similarly to what was proposed by Lillicrap et al. (2019) for the original DDPG, the update of the critic is modulated by an under-relaxation τ using a target network (line 17). At every n_Q iteration, the optimized critic re-evaluates the TD errors of the sampled transitions in \mathcal{D}_L (line 18). Limiting the TD updates for the current batch of trajectories allows for a pseudo-random update of the most critical transitions, according to the critic. In addition, this approach is also computationally cheaper than re-evaluating all the stored transitions in the buffer, usually in the order of magnitude of $\mathcal{O}(10^6)$. Successively, the critic is then used to train the policy in lines 20-24. In this second stage, the gradient with respect to the cost function is computed using eq (4). Note that we use the notation $\Delta \mathbf{w}$ to denote the optimization update for the weights \mathbf{w} , such that the updating reads $\mathbf{w} \leftarrow \mathbf{w} + \Delta \mathbf{w}$. Therefore, the update in a simple gradient descent over a cost function $J(\mathbf{w})$, for example, reads $\Delta \mathbf{w} = -\eta dJ(\mathbf{w})/d\mathbf{w}$. This makes the notation independent of the choice of the optimizer. We note that differently from the original DDPG algorithm in Lillicrap et al. (2019), the updates of the critic and the policy networks are carried out via two separate loops rather than in a single one. In our experiments, we found this approach to lead to more stable model-free policy updates.
- Step 3: Fit random processes for exogenous inputs (line 26).** In principle, both the forward and backward integration of the ODEs driving the digital twin could be carried out using time steps that differ from the ones controlling the interactions with the real system. This would require some interpolation on the exogenous disturbances as well as on the states and the actions. The data storage between forward/backward evaluations could leverage modern checkpointing techniques (see Zhang and Constantinescu 2023). However, keeping the focus on the first proof of concept of the reinforcement twinning idea, we here assume that the numerical integration (both forward and backward) is carried out using the same time stepping from the interaction with the environment (step 1).

Nevertheless, we use the SVR regression on the exogenous input (see 14) to construct the set of random

Algorithm 1.1: Reinforcement Twinning (RT) Algorithm (Part 1)

```

1 Initialize model-free  $\pi_{mf}(\mathbf{w}_{a,mf}^{(0)})$  and model-based policies  $\pi_{mb}(\mathbf{w}_{a,mb}^{(0)})$  and set live policy  $\pi = \pi_{mf}$ 
2 Initialize critic network with weights  $\mathbf{w}_q^{(0)}$  and  $\mathbf{w}'_q^{(0)}$  and targets  $\mathbf{w}'_q$ 
3 Initialize closure function's weights  $\mathbf{w}_p^{(0)}$ 
4 Initialize long term memory buffer  $\mathcal{D}_L$  and short term memory  $\mathcal{D}_S$ 
5 Initialize Step 6 counters and thresholds  $C_\pi, P_\pi, C_w, P_w, T_J$  and  $T_w$ 
6 for  $i = 1, \dots, n_e$  do
7    $\triangleright$  Step 1: Run a real episode
8     for  $k = 1, \dots, n_t$  do
9       Sample  $\xi(i)$ ; if  $\xi(i) \neq 0$ , sample a random action  $\mathbf{n}_k$  from  $\mathcal{N}_n(\mu_a, \Sigma_a)$ 
10      Select action according to policy and exploration noise,  $\tilde{\mathbf{a}}_k = \pi(\tilde{\mathbf{e}}_k; \mathbf{w}_a^{(i)}) + \xi(i)\mathbf{n}_k$ 
11      Act on real system, then collect reward  $r_k$ , states  $\tilde{\mathbf{s}}_{k+1}$  and tracking error  $\tilde{\mathbf{e}}_{k+1}$ 
12      Store error transitions  $(\tilde{\mathbf{e}}_k, \tilde{\mathbf{a}}_k, r_k, \tilde{\mathbf{e}}_{k+1})$  and associated TD errors  $\delta_k$  in  $\mathcal{D}_L$ 
13      Store state transitions  $(\tilde{\mathbf{s}}_k, \tilde{\mathbf{z}}_k, \tilde{\mathbf{a}}_k, \tilde{\mathbf{s}}_{k+1})$  in  $\mathcal{D}_S$ 
14    end
15     $\triangleright$  Step 2: Update Critic and compute the model-free policy update
16      for  $n = 1, \dots, n_Q$  do
17        Sample  $\text{MIN}(n_b, n_t)$  transitions from  $\mathcal{D}_L$  and compute  $\mathcal{J}_q$  and  $d\mathcal{J}_q/d\mathbf{w}_q$  from (7)
18        Compute  $q(\tilde{\mathbf{e}}, \tilde{\mathbf{a}}_k)$  and the update  $\Delta\mathbf{w}_q^{(i)}$ , then update  $\mathbf{w}_q^{(i)} \leftarrow \mathbf{w}_q^{(i)} + \Delta\mathbf{w}_q^{(i)}$ 
19        Use target for  $\tau$  under-relaxation:  $\mathbf{w}_q^{(i)} \leftarrow \tau\mathbf{w}_q^{(i)} + (1 - \tau)\mathbf{w}'_q$  and update target  $\mathbf{w}'_q = \mathbf{w}_q^{(i)}$ 
20        Update the TD errors in the buffer  $\mathcal{D}_L$  for sampled transitions
21      end
22      for  $n = 1, \dots, n_A$  do
23        Sample  $\text{MIN}(n_b, n_t)$  transitions from  $\mathcal{D}_L$ 
24        Compute  $\mathcal{R}_c(\mathbf{w}_a)$  and new set of weights  $\mathbf{w}_{a,mf}^{(n)} \leftarrow \mathbf{w}_{a,mf}^{(n-1)} + \Delta_f\mathbf{w}_{a,mf}$  from  $d\mathcal{R}_c/d\mathbf{w}_{a,mf}$  in (4)
25        Update model-free actor policy:  $\pi_{mf}^{(n)} = \pi_{mf}(\mathbf{w}_{a,mf}^{(n)})$ 
26      end
27     $\triangleright$  Step 3: Prepare inner-episode regressors
28    Use  $n_S$  series of  $\mathbf{z}_k$  from  $\mathcal{D}_S$  use (14) to build  $\mathcal{N}_z^{(l)}(\tilde{\mathbf{d}}[j](t; \boldsymbol{\alpha}[j]), \Sigma[j])$  with  $j \in [1, n_z], l \in [1, n_S]$ 
29     $\triangleright$  Step 4: Optimize digital twin on the  $n_s \times N_z$  virtual episodes with real actions
30    for  $n = 1, \dots, n_G$  do
31      for  $l = 1, \dots, n_S$ , with  $g(\mathbf{s}, \mathbf{w}_p^{(i)})$  do
32        Forward  $N_z$  virtual trajectories with  $\mathbf{s}_0 = \tilde{\mathbf{s}}_0^{(l)}, \mathbf{a}_k$  from  $\tilde{\mathbf{a}}_k^{(l)}, \mathbf{z} \sim \mathcal{N}_z^{(l)}()$ 
33        Compute  $\mathcal{J}_p(\mathbf{w}_p^{(i)})$  in (2) solve  $N_z$  adjoint problems for  $\boldsymbol{\lambda}_p(t_k)$  for each member
34        Compute  $d\mathcal{J}_p/d\mathbf{p}$  from the ensemble (see eq. 10) and the associated updates  $\Delta\mathbf{w}_p^{(l)}$ 
35      end
36      Compute the update  $\mathbf{w}_p^{(i)} \leftarrow \mathbf{w}_p^{(i)} + \Delta\mathbf{w}_p^{(i)}$ 
37    end
38    Save current optimal set of  $\mathbf{w}_p = \mathbf{w}_p^*$ 
39    ...
40  end

```

processes (here treated as Gaussian processes) from which the ensemble of possible realizations of the (stochastic) exogenous input will be sampled. These are used for ensemble averaging of the gradient over possible trajectories. For each of the trajectory $l \in [1, n_S]$ available in the short-term memory

Algorithm 1.2: Reinforcement Twinning (RT) Algorithm (Part 2)

```

37 ▷ Step 5: Run  $N_z$  virtual episodes with current policy and compute model-based policy update ...
38   for  $n = 1, \dots, n_{mb}$  with  $g(\mathbf{s}, \mathbf{w}_p^*)$  do
39     Forward  $N_z$  virtual trajectories with  $\mathbf{s}_0 = \check{\mathbf{s}}_0^{(l)}$ ,  $\mathbf{a}_k = \pi_{mb}(\mathbf{s}_k; \mathbf{w}_a^{(i)})$ ,  $\mathbf{z} \sim \mathcal{N}_z^{(l)}()$ 
40     Compute  $\mathcal{J}_a(\mathbf{w}_a^{(i)})$  in (3) and solve  $N_z$  adjoint problems to get  $\lambda_a(t_k)$  for each member
41     Compute  $d\mathcal{J}_a/d\mathbf{a}$  from the ensemble (see eq. 12)
42     Compute the new set of weights  $\mathbf{w}_{a,mb}^{(n)} \leftarrow \mathbf{w}_{a,mb}^{(n-1)} + \Delta\mathbf{w}_a^{(l)}$ 
43     Update model-based actor policy  $\pi_{mb}^{(n)} = \pi_{mb}(\mathbf{w}_{a,mb}^{(n)})$ 
44   end
45   Save current optimal set of  $\mathbf{w}_{a,mb} = \mathbf{w}_{a,mb}^*$ 
46   ▷ Step 6: Policy switching and parametrization cloning
47   Forward  $N_z$  virtual trajectories with  $\mathbf{s}_0 = \check{\mathbf{s}}_0^{(l)}$ ,  $\mathbf{a}_k = \pi_{live}(\mathbf{s}_k, \mathbf{w}_{a,live})$ ,  $\mathbf{z} \sim \mathcal{N}_z^{(l)}()$ . Get  $\bar{\mathcal{J}}_{a,live}$ 
48   Forward  $N_z$  virtual trajectories with  $\mathbf{s}_0 = \check{\mathbf{s}}_0^{(l)}$ ,  $\mathbf{a}_k = \pi_{idle}(\mathbf{s}_k, \mathbf{w}_{a,idle})$ ,  $\mathbf{z} \sim \mathcal{N}_z^{(l)}()$ . Get  $\bar{\mathcal{J}}_{a,idle}$ 
49   Policy switching and weight cloning based on the decision tree (Figure 3)
50 end

```

buffer \mathcal{D}_S , we denote as $\mathbf{z}^{(l)} \sim \mathcal{N}_z^{(l)}()$ a sample of the Gaussian processes generating the evolution of possible exogenous inputs.

- **Step 4: Optimize digital twin on the real actions (lines 27-36).** The goal of this step is to find the closure parameters \mathbf{w}_p such that the digital twin’s prediction matches with the n_S trajectories of the real system, stored in \mathcal{D}_S . Consequently, the loss function \mathcal{J}_p in (2) is minimized using a gradient-based optimization loop. This consists of n_G iterations and computes the updates $\Delta\mathbf{w}_p$ from the gradient evaluated along the n_S trajectories available in \mathcal{D}_S . Again, fixing the numerical time stepping to the one of the real interaction avoids the need for action interpolation, but might become problematic for stiff problems. For each trajectory (loop in lines 27-33), a total of N_z possible realizations of the exogenous input are considered (sampled from the processes $\mathcal{N}_z^{(l)}$ from the previous step), and the gradient is computed using the adjoint method (see eq. 10). The associated updates are then averaged (line 32), and the optimization step is carried out (line 34). Each optimization step requires a total of $n_S \times N_Z$ forward and backward virtual episodes.
- **Step 5: Model-based policy update. (lines 37-43).** This step is structurally similar to the previous: it computes the ensemble-averaged adjoint-based gradient (line 41) of a cost function (\mathcal{J}_a) and performs a number (n_{mb}) of gradient-based optimization steps (line 43). In this case, however, the interactions with the digital twin follow the model-based policy π_{mb} instead of the actions stored in \mathcal{D}_S . This allows to evaluate the current set of model-based policy weights $\mathbf{w}_{a,mb}$. The response of the digital twin is governed by the closure law defined by the current best set of weights, i.e. $\mathbf{p} = g(\mathbf{s}, \mathbf{w}_p^*)$.
- **Step 6: Policy switching and parametrization cloning. (lines 44-47).** This step decides which of the policies π_{mb} or π_{mf} becomes “live” and which one becomes “idle”. The first is deployed in the next interaction with the real system, while the second continues to be trained with different mechanisms. The decision in this step is based on the policy performances in the virtual environment, evaluated and averaged over N episodes with randomized initial conditions and disturbances. Defining as $\bar{\mathcal{J}}_{a,live}$ and $\bar{\mathcal{J}}_{a,idle}$ the averaged cost functions for the “live” and “idle” policies, we introduce a tolerance factor $T_J \in \mathbb{R}$, a threshold $P_\pi \in \mathbb{N}$, and a counter $C_\pi \in \mathbb{N}$ to avoid overly impulsive decisions. If the live policy performs worse than the idle one more than the tolerance factor ($\bar{\mathcal{J}}_{a,live}/\bar{\mathcal{J}}_{a,idle} < T_J$), the counter C_π gets incremented. If C_π exceeds the threshold P_π , the idle policy takes over and becomes the live one. On the other hand, if the opposite is true, then we check that the idle policy did not

happen to be stuck in a local minima, analyzing its weight variation:

$$d\mathbf{w}_a = \frac{\|\mathbf{w}_a^i - \mathbf{w}_a^{i-1}\|}{\|\mathbf{w}_a^i\|}, \quad (16)$$

where i indicates the current number of the episode ($i \in [1, n_e]$). To this end, we introduce a tolerance T_w , a counter C_w and a threshold P_w and repeat the previous decision process: if $d\mathbf{w}_a$ falls below T_w , C_w increases. If C_w goes beyond P_w , it is reasonable to assume that the policy optimization step is trapped in a local minimum, and we replace the “idle” parametrization by cloning the “live” one. The decision tree of this step is recalled in Figure 3.

We close with a few general remarks on the algorithms.

Remark 1. In Steps 4 and 5, the n_S hyperparameters define how much the digital twin should consider past experiences. In this work, we set $n_S=1$, thus focusing on the last trajectory solely, while having a variable N_z to promote robustness against randomness on the exogenous inputs and take into account possible sampling errors which may occur in real-world scenarios.

Remark 2. The idle policy continues its training through different mechanisms. No special considerations are needed if the idle policy is the model-based policy: this continues to be trained on the digital twin regardless of whether it is active on the real system or not. On the other hand, if the idle policy is model-free, the learning occurs indirectly through two mechanisms that establish a “demonstration” from the model-based to the model-free: (1) the storage of transitions in the memory buffer \mathcal{D}_L and (2) the continuous training of the value function Q . The off-policy nature of the reinforcement learning algorithm here implemented allows the agent to learn from policies that are exploratory or simply not “optimal”, according to the current Q function. In this case, when the model-free policy is idle, and the Q function continues to be updated by observing the model-based policy in action on the real system, a sort of “demonstration” mechanism is established. The fact that the model-free could learn by the demonstration and eventually overtake the lead as a live policy is arguably the most significant contribution of this work.

Remark 3. The model-free update (Step 2), the model-based update (Steps 3,4,5), and the individual evaluations occurring in (Step 6) are independent processes and can be parallelized, greatly reducing computational time.

5. Selected Test Cases

We present the three selected test cases: (1) the control of a wind turbine subject to time-varying wind speed (Section 5.1), (2) the trajectory control of flapping-wing micro air vehicles (FWMAVs) subject to wind gusts (Section 5.2) and (3) the mitigation of thermal loads in the management of cryogenic storage tanks (Section 5.3). These are very simplified versions of the real problems, and the reader is referred to the specialized literature for more details.

5.1. Wind Turbine Control

Test case description and control problem. We consider the problem of regulating the rotor’s angular speed ω_r and the extracted power P_e of a variable speed variable pitch horizontal turbine of radius R , subject to time-varying wind velocity u_∞ (see Laks et al. 2009; Pao and Johnson 2009).

The operation (and thus the control objectives) of a wind turbine depends on the wind speed in relation to three regions, identified by three velocities: cut-in (u_{ci}), rated (u_r) and cut-out (u_{co}) wind speeds. These are shown in Figure 4 for the NREL 5-MW turbine considered in this test case (details in the following subsection). In region 1 ($u_\infty < u_{ci}$), the wind speed is too low to justify the turbine operation and no power is produced. In region 2 ($u_{ci} < u_\infty < u_r$), the goal is to maximize the energy production. This is usually achieved by pitching the blades at the optimal value β^* and acting on the generator torque to keep the optimal rotational speed. In region 3 ($u_\infty > u_r$), the turbine is in above-rated conditions, and the goal is

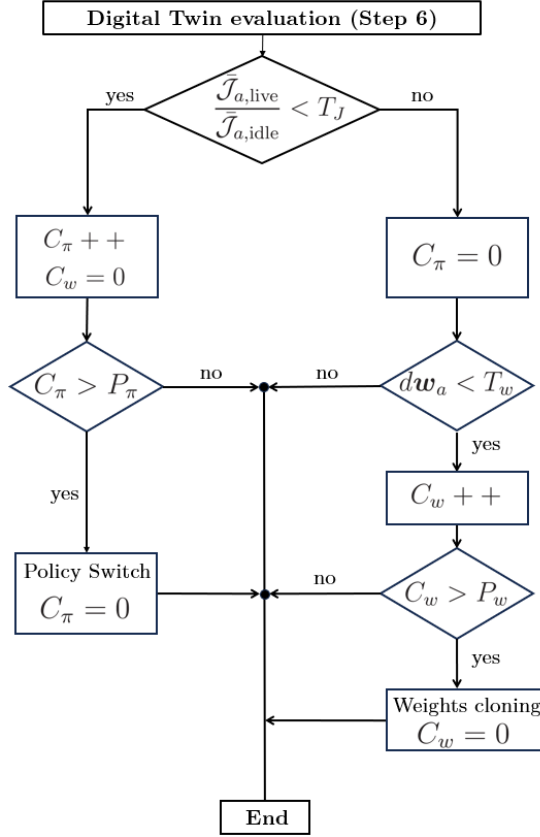
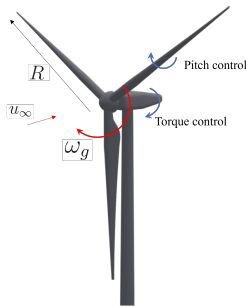
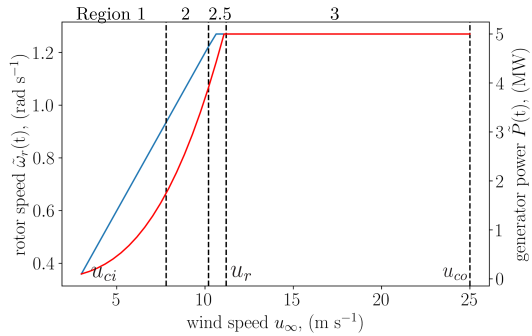


Figure 3: Decision tree in step 6 of the Reinforcement Twinning algorithm (see 1.1. This step defines 1) which of the model-free or model-based policy becomes live and idle and 2) whether one of the two is consistently under-performing and is thus replaced by a clone of the other.

to keep the power extraction at its nominal value P_N , thus reducing the aerodynamic load acting on the rotor. This is usually achieved by keeping the nominal generator torque and acting on β . Finally, the wind turbine is shut down if $u_\infty > u_{co}$, preventing mechanical and electrical overloading. Particularly critical is



(a)



(b)

Figure 4: Sketch of the main parameters involved in wind turbine control (4a) and reference power curve (4b), \tilde{P} (in red), and rotor speed $\tilde{\omega}_r$ (in blue).

the transition between regions 2 and 3 (region 2.5 in Fig.4,) where gusts or lulls could result in shifting of

operating conditions, leading to conflicting requirements between torque and pitch controllers. This region is typically handled via set point smoothing, mitigating transients when switching from one control logic to another (Bianchi et al., 2007; Abbas et al., 2020).

In this test case, we combine a Maximum Power Point Tracking (MPPT) controller in below-rated conditions (Bhowmik and Spee, 1999; Howlader et al., 2010) with a regulation control in above-rated conditions. The controller can act on both the generator torque and the pitch angle, receiving as sole input the generator speed ω_g , as typically done in multi-megawatt wind turbines (Jonkman et al., 2009). The current wind speed u_∞ acts as exogenous input, which we assume can be provided by real-time measurements. We thus collect a sequence $u_\infty(t_k)$ with $t_k = k\Delta t$. To avoid high-frequency excitation of the system, we filter the generator speed signal using an exponential smoothing (Zheng and Jin, 2022) with the recursive relations:

$$\hat{y}(t_k) = (1 - \alpha)y(t_k) + \alpha \cdot y(t_{k-1}), \quad (17)$$

with α being the low-pass filter coefficient computed as $\alpha = \exp(-2\pi f_c \Delta t)$, with f_c the minimum cut-off frequency, y the generic raw signal and \hat{y} its low-pass filtered version.

We employ this filter for the generator rotational speed, ω_g and the measured wind speed, u_∞ . From the latter, it is possible to define the target rotational speed $\tilde{\omega}_g$ and extracted power \tilde{P} from the reference curves in Figure 4. In Region 2, these two variables are linked by the operating conditions, while in Region 3, these are defined by mechanical constraints. In below-rated conditions, the power is theoretically maximized if the rotor operates at its optimal tip-speed-ratio $\lambda_{r,*} = \omega_r R / u_\infty$. Thus, one can define the reference generator speed relying on the measured wind speed as

$$\tilde{\omega}_g = N_g \frac{\lambda_{r,*} \hat{u}_\infty}{R}, \quad (18)$$

where N_g is the gearbox ratio. This variable is constrained in the range $\omega_{g,min} \leq \tilde{\omega}_g \leq \omega_{g,rated}$, taking into account the machine specifications. Therefore, given $\tilde{\omega}_g$ the target rotational velocity, we define the tracking errors as $e_1(t) = (\tilde{\omega}_g - \omega_g) / \gamma_1$, and its integral over the past rotor revolution, $e_2(t) = (\int_{t_i - T_r}^{t_i} e(t') dt') / \gamma_2$, where $\gamma = [\gamma_1, \gamma_2]$ ensure that both inputs lie in $[-1, 1]$, and consider these as the inputs of the control logic. We then define the actuation vector as

$$\mathbf{a}(e(t), \mathbf{w}_a) = \begin{bmatrix} \tau_g \\ \beta \end{bmatrix} = \begin{cases} \text{clip}(w_{a1}e_1(t) + w_{a2}e_2(t), \tau_{g,min}, \tau_{g,max}) \\ \text{clip}(w_{a3}e_1(t) + w_{a4}e_2(t), \beta_{min}, \beta_{max}) \end{cases} \quad (19)$$

where $\text{clip}(x, x_1, x_2)$ is a smooth step returning x_1 if $x < x_1$, x if $x_1 < x < x_2$ and x_2 if $x > x_2$. In this work, we define it as

$$\text{clip}(x, x_1, x_2) = \frac{1}{2}(\tanh(x) + 1)(x_2 - x_1) + x_1, \quad (20)$$

though any differentiable smooth step fits the purposes of bounding the action space while ensuring differentiability. This allows to limit the actuations rate of change according to the actuators' specifications, $\dot{\tau}_{g,max}$ and $\dot{\beta}_{max}$. We further assume that the controller can be informed by measurements of the turbine's rotational velocity $\tilde{\omega}$ and the generator torque $\tilde{\tau}_g$. It is thus possible to define a tracking error on the power as $e_P = \tilde{\tau}_g \cdot \omega(t; \mathbf{w}_a) - \tilde{P}$ and use this signal to measure the controller's performance. The reference power \tilde{P} follows the $K\omega^2$ -law (Bossanyi, 2000) in under-rated conditions, setting

$$\tau_g(t) = K\omega_g(t) \quad K = \frac{\pi\rho R^5 C_{p,max}}{2\lambda_{r,*}^3 N_g^3}, \quad (21)$$

with

$$\tilde{P} = K\omega_g(t)^3. \quad (22)$$

The target power production, also accounting for Region 3, is this $\tilde{P} = \text{MIN}(P_N, K\omega_g(t)^3)$. Combining these two references, the cost function driving the model-based optimal control law is

$$\mathcal{J}_a = \frac{\alpha_1}{2 T_o} \int_0^{T_o} e_1(t)^2 dt + \frac{\alpha_2}{2 T_o} \int_0^{T_o} e_P(t)^2 dt, \quad (23)$$

while the for model-free counterpart, we define the reward as

$$\mathcal{R}_a = -\frac{\alpha_1}{2 n_t} \sum_{k=0}^{n_t-1} e_1^2(t_k) - \frac{\alpha_2}{2 n_t} \sum_{k=0}^{n_t-1} e_P^2(t_k). \quad (24)$$

where α_1 and α_2 ensure that the two components of the cost function have comparable orders of magnitude. The choice of including both the velocity *and* the power extraction is justified by the fact that these parameters are independent, in the sense that one could extract the same amount of power with different generator velocities by acting on the torque, possibly violating mechanical constraints.

Selected conditions and environment simulator. Disregarding aeroelastic effects on both the blades and the tower, the simplest model of the rotor dynamics is provided by the angular momentum balance, which leads to a first-order system for the turbine’s generator angular speed ω_g :

$$\dot{\omega}_g = \frac{N_g}{J} (\tau_a - \tau_g N_g), \quad (25)$$

where J is the rotor’s moment of inertia, τ_a is the aerodynamic torque, τ_g is the opposing torque due to the generator and the gear train, and N_g the gearbox ratio. The gearbox efficiency is assumed to be unitary. The aerodynamic torque is linked to the wind velocity as

$$\tau_a = \frac{1}{2} \rho A_r \frac{C_p(\lambda_r, \beta)}{\omega_r} u_\infty^3, \quad (26)$$

where ρ is the air density, $A_r = \pi R^2$ the turbine’s swept area, and $C_p = P_e/(1/2\rho A u_\infty^3)$ is the power coefficient, that is the ratio between the extracted power P_e and the available one. For a given turbine design, this coefficient is a function of the tip-speed ratio λ_r and the blade pitching angle β . A predictive model can thus be obtained by combining (25) and (26) and a pre-computed $C_p(\lambda_r, \beta)$ map. This map is usually obtained via Blade Element Momentum Theory (BEMT, Moriarty and Hansen 2005), and we do the same for simulating the real environment in this test case. The resulting map for the selected turbine is shown in Figure 5b.

We consider the NREL 5-MW reference offshore wind turbine (Jonkman et al., 2009). This turbine has $R = 63$ m, $J = 115926$ kg m² and $\omega_{r,\text{rated}} = 1.27$ rad s⁻¹ for $u_\infty \geq 11.4$ m s⁻¹. The gearbox ratio is $N_g = 97$. The actuation bounds of the pitch angle and torque actuators are respectively $(\beta_{\min}, \beta_{\max}) = (0, 90)$ deg and $(\tau_{\min}, \tau_{\max}) = (0, 43093)$ Nm. Their maximum rate of change are $\dot{\beta}_{\max} = 8$ deg s⁻¹ and $\dot{\tau}_{g,\max} = 15000$ N m s⁻¹, respectively. From these, we define the cut-off frequency as the harmonic associated with the highest rate of change, obtaining $f_{c,\tau} = 0.05$ Hz and $f_{c,\beta} = 0.04$ Hz. We set the filter smoothing coefficient according to the slowest pitch actuator, finding $\alpha = 0.98$.

We take $T_o = 600$ s for the observation time and assume a sampling of $f_s = 4$ Hz for all the simulated instrumentation. We simulate the incoming wind speed time series using the stochastic, turbulent wind simulator TurbSim (Jonkman, 2006) considering a wind velocity with average $u_\infty = 11$ m s⁻¹ and turbulence intensity TI= 16%, thus oscillating between below and above rated. An example of velocity time series is shown in Figure 5b together with its filtered signal.

Digital Twin definition. The wind energy community has put significant effort into the development of digital twins of onshore and offshore wind turbines, with applications ranging from load estimations (Pimenta et al., 2020; Branlard et al., 2023) to real-time condition monitoring (Olatunji et al., 2021; Fahim et al., 2022). In this work, we solely focus on the rotor’s aerodynamic performance and the twinning process seeks to identify a closure law for the power coefficient from data, starting from (25) and (26). In fact, the BEMT, commonly used to obtain the C_p curve, assumes that the flow is steady, and this is questionable in the presence of large fluctuations in the wind speed (Leishman, 2002). Moreover, the coefficient can change

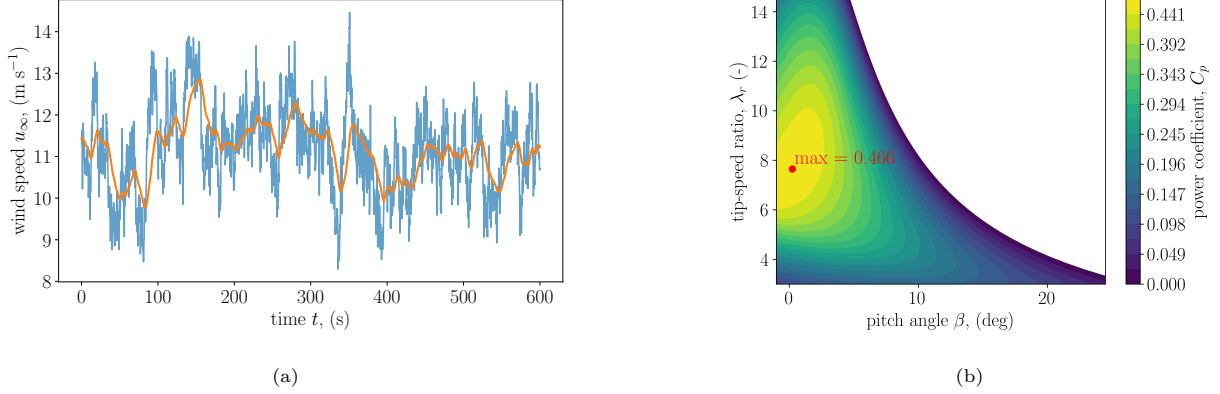


Figure 5: Fig 5a): sample of the wind speed (exogenous input) considered for the test case 1, unfiltered (in blue) and filtered (orange). Fig 5b) shows the contour of the power coefficient $C_p(\lambda_r, \beta)$ for the NREL 5MW turbine considered for control purposes. The controller’s objective is to keep the turbine near the maximum ($C_p = 0.46$) acting on the motor torque or the blade pitching.

over time as a result of turbine wear (e.g. due to blade erosion) or in the presence of extreme conditions (e.g. ice, dirt or bug buildup) Staffell and Green (2014). This is why any strategy based on a pre-computed C_p curve is likely sub-optimal (Johnson, 2004, 2006) and the idea of continuous updates of this closure law from operational data has merit. Although this exercise is purely illustrative, the approach can be readily extended to more complex and multi-disciplinary model formulations.

The digital twin employs the power coefficient parametrization formulated by Saint-Drenan et al. (2020)

$$\begin{cases} C_p(\lambda_r, \beta) = c_1 \left(\frac{c_2}{\xi} - c_3\beta - c_4\xi\beta - c_5\beta^{c_{12}} - c_6 \right) e^{-\frac{c_7}{\xi}} + c_8\xi \\ \xi^{-1} = (\lambda_r + c_9\beta)^{-1} - c_{10}(\beta^3 + 1)^{-1} \end{cases} \quad (27)$$

with the parameters $\mathbf{w}_p = [c_1, c_2, \dots, c_{12}]$ to be identified. This model is known to be valid up to a maximum pitch excursion of $\beta = 30$ deg. Therefore, we limit the maximum allowable pitch command to this value in our experiments.

The assimilation optimizes for \mathbf{w}_p , aiming to minimize the error between the predicted dynamics $\omega_g(t)$ and the real system behaviour $\tilde{\omega}_g(t)$. This translates into minimizing the cost function

$$\mathcal{J}_p = \frac{1}{2} \int_0^T \left(\omega(t; \mathbf{w}_p) - \tilde{\omega}(t) \right)^2 dt. \quad (28)$$

5.2. Trajectory control of flapping wings micro air vehicles

Test case description and control problem. This test case considers the control of a Flapping-Wing Micro Air Vehicle (FWMAV) which aims to move from one position to another in the shortest possible time. FWMAVs are sometimes considered better alternatives to fixed-wing and rotary-wing micro aerial vehicles because of their higher agility and manoeuvrability (Haider et al., 2020). The design and control of these drones seek to mimic the remarkable flight performances of hummingbirds, which can undertake complex manoeuvres with an impressive response time (see, for example, Cheng et al. 2016 and Ortega-Jiménez and Dudley 2018).

Reproducing these performances requires advanced knowledge of the flapping wing’s aerodynamics in the low Reynolds number regime, as well as the fluid-structure interaction resulting from the wing’s flexibility. These remain significant challenges for advanced numerical simulations (Fei et al., 2019; Xue et al., 2023). The proposed test case shows how simplified models of the wing’s aerodynamics could be derived in real-time while an FWAVs seeks to achieve its control target. The considered problem is illustrated in Figure 6a. A drone initially at $\mathbf{x}_0 = [x_0, z_0]$ m and $\dot{\mathbf{x}}_0 = 0$ m/s is requested to move to $\tilde{\mathbf{x}}_f = [\tilde{x}_f, \tilde{z}_f]$ m as fast as possible,

and then hover in that position, i.e. $\dot{\tilde{\mathbf{x}}}_f = [0, 0]$, by continuously adapting its flapping wing motion. We challenge the controller by introducing gusty wind disturbances \mathbf{u}_∞ ,

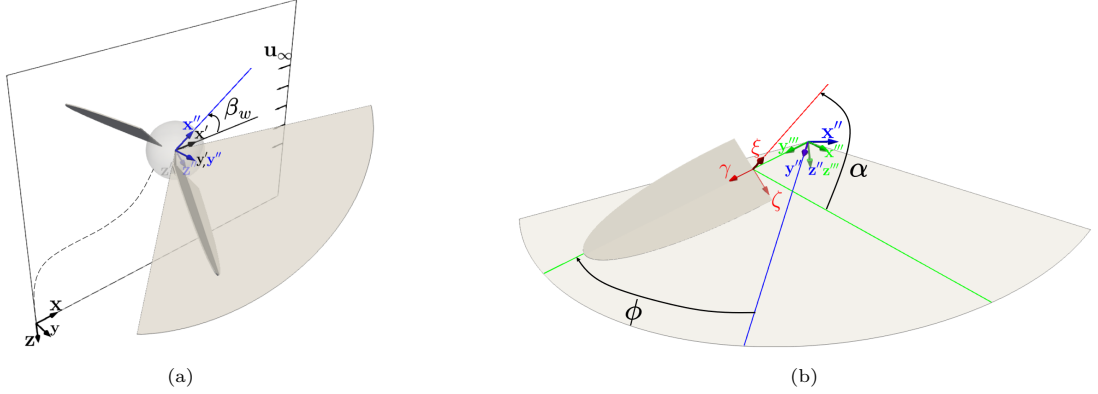


Figure 6: (a) Schematic of the flapping drone going from the initial position $\tilde{\mathbf{x}}_0$ to the final position $\tilde{\mathbf{x}}_f$. $(x'y'z')$ is the stroke frame that is tilted by β_w from the inertial frame (xyz) (b) Zoom on the stroke plane that holds three frames (stroke frame $x'y'z'$, flapping plane $x''y''z''$ and the wing-fixed frame (ξ, γ, ζ)) which defines the flapping angle ϕ and the pitching angle α . The wing frame is offset on the wing root only for the clarity of the figure.

To simplify the body's kinematics, we consider only 2D trajectories characterized by the position vector $\mathbf{x}(t)$ defined in the ground frame (x, y, z) . We also attach a moving frame (x', y', z') to the body with no rotational freedom. Starting from the body frame, three Euler angles (β_w, ϕ, α) and three reference frames characterize the wing kinematics (Figure 6b). The wings always flap symmetrically so that the position of one wing defines the other one.

The body frame is first pitched by a stroke plane angle $\beta_w(t)$ along y' to define the stroke plane frame (x'', y'', z'') . The wing tips are constrained to flap in the stroke plane (x'', y'') as it flaps along the normal z'' . The flapping frame (x''', y''', z''') follows this rotational motion and defines the flapping angle $\phi(t)$ between the wing symmetry axis y''' and the lateral direction y'' (Figure 6b). The last frame is the wing-fixed frame (ξ, γ, ζ) that results from the pitching rotation along the wing symmetry axis. The pitching angle $\alpha(t)$ is then defined between the chord-normal direction ξ and the stroke plane axis x''' . The reader is referred to Whitney and Wood (2010) and Cai et al. (2021) for a complete treatment of the flapping wing kinematics. We select an harmonic parametrization for ϕ and α :

$$\phi(t) = A_\phi \cos(2\pi ft) \quad \text{and} \quad \alpha(t) = A_\alpha \sin(2\pi ft), \quad (29)$$

where the beginning of the stroke ($t = 0$) is when the flapping amplitude is maximal ($\phi(t) = A_\phi$) and the chord plane is perpendicular to the stroke plane ($\alpha(t) = 0^\circ$).

We assume that the flapping frequency f and the pitching amplitude A_α are fixed and set the flapping amplitude A_ϕ as a control parameter together with the stroke plane angle β_w , i.e. $\mathbf{a} = [A_\phi, \beta_w]^T$. We link the action vector to the state error using a Proportional–Derivative (PD) controller with an offset and capped outputs:

$$\mathbf{a}(\mathbf{e}; \mathbf{w}_a) = \begin{cases} \text{clip}(w_{a1} + w_{a2}e_x + w_{a3}e_z + w_{a4}\dot{e}_x + w_{a5}\dot{e}_z, A_{\phi, \min}, A_{\phi, \max}) \\ \text{clip}(w_{a6} + w_{a7}e_x + w_{a8}e_z + w_{a9}\dot{e}_x + w_{a10}\dot{e}_z, \beta_{w, \min}, \beta_{w, \max}) \end{cases} \quad (30)$$

where $\mathbf{e} = [e_x, e_z, \dot{e}_x, \dot{e}_z]$, with $e_x = x_f - x$, $e_z = z_f - z$ and dots denoting differentiation in time. The control action parameters are $\mathbf{w}_a \in \mathbb{R}^{10}$ and the function $\text{clip}(x, x_1, x_2)$ is the smoothing operation introduced in (20). The bias terms w_{a1}, w_{a6} helps stabilize the drone in hovering conditions once the target position is reached since this operation requires a continuous effort even when the state error is zero.

The reward function driving the model-free controller is written as

$$\mathcal{R}_c = -\frac{1}{2n_t} \sum_{k=1}^{n_t} \|\check{\mathbf{e}}_k\|_2^2 + \alpha_1 \|\dot{\check{\mathbf{e}}}_k \circ \mathbf{h}(\mathbf{x}_k)\|_2^2. \quad (31)$$

where \circ denotes the Hadamard (entry by entry) product and $\mathbf{h}(\mathbf{x}_k)$ is a vector of two Gaussian functions with mean \mathbf{x}_f and standard deviation $\sigma = 0.71$:

$$\mathbf{h}(\mathbf{x}_k) = \frac{\mathbf{x}_f^2}{2} \exp\left[-\frac{1}{2} \left(\frac{\mathbf{x}_k - \mathbf{x}_f}{\sigma}\right)^2\right] \quad (32)$$

This function is zero far from the target position and unitary once the drone reaches it, so the role of the second term in (31) is to penalize large velocities once the drone approaches the goal. The term $\alpha_1 \in \mathbb{R}$ in (31) weights the importance of the penalty. The cost function driving the model-based controller reproduces the same approach in a continuous domain and reads:

$$\mathcal{J}_a = \frac{1}{2T_0} \int_0^{T_0} \|\mathbf{e}(t)\|_2^2 + \alpha_1 \|\dot{\mathbf{e}}(t) \circ \mathbf{h}(\mathbf{x}(t_k))\|_2^2 dt. \quad (33)$$

Selected conditions and environment simulator. We consider a drone with mass $m_b = 3$ g and a constant flapping frequency of $f = 20$ Hz. Given the initial position $\mathbf{x}_o = [0, 0]$ m, we set the target position at $\mathbf{x}_f = [5, 5]$ m. We assume that the manoeuvre should take less than $n_t = 100$ flapping cycles, hence we consider an observation time of $T_o = 5$ s. This defines the observation time for the twinning. We fix the pitching amplitude to $A_\alpha = 45$ deg and let the flapping amplitude vary in the range $A_\phi \in [50; 88]$ (deg). These values are comparable to what is observed in hummingbird's flight, although the harmonic parameterization in (29) oversimplifies their actual wing dynamics (Kruyt et al., 2014). The stroke plane angle is bounded in the range $\beta_w \in [-30, 30]$ (deg).

We assume that the drone's wings are semi-elliptical and rigid with a span $R = 0.05$ m and a mean chord $\bar{c} = 0.01$ m. The wing roots are offset of $R_0 = 0.0225$ m from the body barycenter, which is also the centre of rotation of the wings. We decouple their motion from the body such that the wing inertia does not influence the body motion (Taha et al., 2012). This hypothesis simplifies the body dynamics, which becomes only a function of the aerodynamic forces produced by the wings and the gravitational force. These are assumed to apply on the barycenter of the body, which is treated as a material point. Therefore, restricting the dynamics to the (x, z) plane, the force balance gives

$$m_b \ddot{x} = F_{x,w} - D_b \cos(\beta_b) \quad (34)$$

$$m_b \ddot{z} = F_{z,w} - m_b g - D_b \sin(\beta_b) \quad (35)$$

where the subscript w refers to forces produced by the wing and the subscript b identifies body quantities. Hence the aerodynamic forces produced by the flapping wings are $\mathbf{F}_w = [F_{x,w}, F_{z,w}]^T$, D_b is the magnitude of the drag force exerted on the body and β_b is the angle between the drag force and the x axis. Considering the velocity of the drone $\dot{\mathbf{x}} = [\dot{x}, \dot{z}]^T$ and the incoming horizontal wind disturbance (both in the ground frame), this angle is defined as $\beta_b = \tan^{-1}(\dot{z}/(\dot{x} + u_\infty))$. The magnitude of the drag force is computed as

$$D_b = \frac{1}{2} \rho S_b C_{D,b} U_b^2, \quad (36)$$

where ρ is the air density, $S_b = 0.0005$ m² is the body's cross-sectional area, $C_{D,b}$ is the body's drag coefficient, here taken as unitary, and U_b is the modulus of the relative velocity between the drone body and the wind, i.e. $U_b = \sqrt{(\dot{x} + u_\infty)^2 + \dot{z}^2}$. The wind disturbance u_∞ results from a stationary Gaussian process with mean value $\bar{u}_\infty = 1$ m/s, in opposite direction to the x versor, and covariance matrix defined by a Gaussian kernel $\kappa(u_\infty(t), u_\infty(t + \tau)) = \exp(-\tau^2/(2\sigma_f^2))$ with $\sigma_f = 3$ s.

To compute the wing forces in (34) and (35) we follow the semi-empirical quasi-steady approach of Lee et al. (2016), based on the work by Dickinson et al. (1999). This is a common approach in control-oriented investigations (see e.g. Cai et al. (2021); Fei et al. (2019)) because it provides a reasonable compromise

between accuracy and computational cost, at least for the case of smooth flapping kinematics and near hovering conditions (see Lee et al. (2016)).

The approach is based on Blade Element Momentum Theory (BEMT), which partitions the wing into infinitesimal elements (see Figure 7a). Each element produces an infinitesimal aerodynamic force that must be integrated along the span to get the total lift and drag. In the case of the smooth flapping motion (29), the forces due to the flapping motion dominate all the other physical phenomena (Lee et al. (2016)) so that the lift L_w and drag D_w expressions are

$$L_w(t) = \frac{1}{2}\rho C_{L,w}(\alpha) \int_{\Delta R}^R U_w^2(t,r)c(r)dr \quad (37)$$

$$D_w(t) = \frac{1}{2}\rho C_{D,w}(\alpha) \int_{\Delta R}^R U_w^2(t,r)c(r)dr, \quad (38)$$

where $C_{L,w}$ and $C_{D,w}$ are the lift and drag coefficient of the wing and U_w is the modulus of the relative velocity between the wing displacement, the body displacement and the wind. This velocity depends on the span-wise coordinate of the wing section r (see Figure 7b) and is computed as

$$\mathbf{U}_w(r, t, \mathbf{u}) = [\mathbf{U}_{w,x}, \mathbf{U}_{w,y}, \mathbf{U}_{w,z}] = \left(\mathbf{R}_2(\alpha) \begin{bmatrix} 0 \\ 0 \\ \dot{\phi} \end{bmatrix} \right) \times \begin{bmatrix} 0 \\ r \\ 0 \end{bmatrix} + \mathbf{R}_2(\alpha)\mathbf{R}_3(\phi)\mathbf{R}_2(\beta_w) \left(\begin{bmatrix} \dot{x} \\ \dot{y} \\ 0 \end{bmatrix} + \begin{bmatrix} U_{wi} \\ 0 \\ 0 \end{bmatrix} \right) \quad (39)$$

The first term is the (linear) flapping velocity of the wing, while the second term gathers the velocity of the body and the wind. Both terms are projected in the wing frame thanks to three rotation matrices:

$$\mathbf{R}_2(\alpha) = \begin{bmatrix} \cos(\alpha) & 0 & \sin(\alpha) \\ 0 & 1 & 0 \\ -\sin(\alpha) & 0 & \cos(\alpha) \end{bmatrix} \quad \mathbf{R}_3(\phi) = \begin{bmatrix} \cos(\phi) & \sin(\phi) & 0 \\ -\sin(\phi) & \cos(\phi) & 0 \\ 0 & 0 & 1 \end{bmatrix} \quad (40a)$$

$$\mathbf{R}_2(\beta_w) = \begin{bmatrix} \cos(\beta_w) & 0 & \sin(\beta_w) \\ 0 & 1 & 0 \\ -\sin(\beta_w) & 0 & \cos(\beta_w) \end{bmatrix} \quad (40b)$$

where $\mathbf{R}_2(\beta_w)$ transform velocities from the (x', y', z') frame to the (x'', y'', z'') frame, $\mathbf{R}_3(\phi)$ from (x'', y'', z'') to (x''', y''', z''') and $\mathbf{R}_2(\alpha)$ from (x''', y''', z''') to (ξ, γ, ζ) .

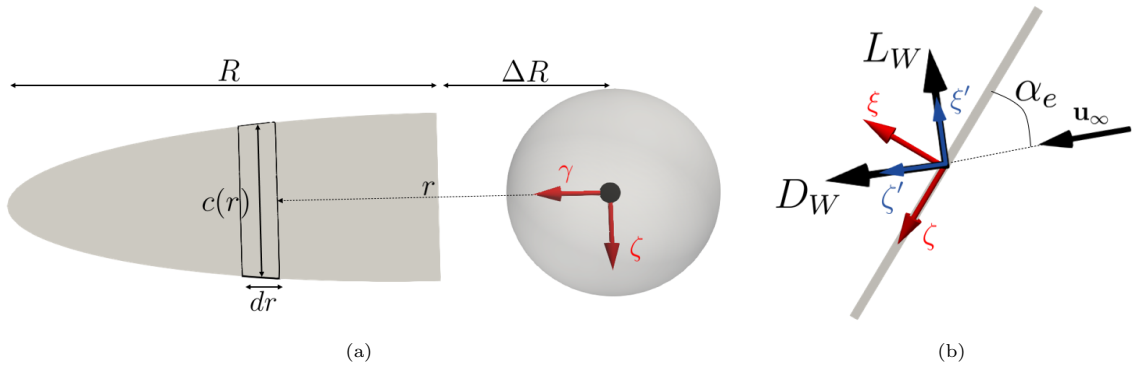


Figure 7: (a) Main dimensions of the semi-elliptical wing. An element part of the BET is also highlighted (b) Effective angle of attack α_e , lift L_w and drag D_w shown with the wind frame (ξ', γ', ζ') and wing-fixed frame (ξ, γ, ζ) on a chord section of the wing

The force coefficients $C_{L,w}$ and $C_{D,w}$ in equations 37 and 38 are modeled similarly to Lee et al. (2016) and Sane and Dickinson (2001):

$$C_{L,w} = a \sin(2\alpha_e) \quad (41)$$

$$C_{D,w} = b + c (1 - \cos(2\alpha_e)), \quad (42)$$

where $\mathbf{w}_p = [a, b, c]$ are the closure parameters for this problem. This parametrization approximates the influence of the Leading Edge Vortex (LEV), generated at a high pitching angle due to flow separation and stably attached on the suction side (see Sane (2003)). The corresponding force coefficients depend on the effective angle of attack $\alpha_e = \cos^{-1}(U_{w,z}/\|\mathbf{U}_w\|_2)$, defined between the chord direction ζ and the relative velocity of the wing \mathbf{U}_w .

Finally, the forces in equations (37) and (38) were computed in the reference wind frame (ξ', γ', ζ') , which rotates the wing frame by α_e along γ . The drag D_w is then aligned with ξ' while the lift is perpendicular to the drag (Figure 7b). These forces are successively transformed into the wing frame and then into the body frame to retrieve $F_{x,w}$ and $F_{z,w}$ in the dynamic equations (34) and (35).

In this test case, the real environment is simulated using $\mathbf{w}_p = [a, b, c] = [1.71, 0.043, 1.595]$ in (37) and (38), as approximated from (Lee et al., 2016) for semi-elliptical wings. For the digital twin, these are the parameters to be identified while interacting with the environment to minimize the cost function:

$$\mathcal{J}_p = \frac{1}{2} \int_0^T (\mathbf{s}(t; \mathbf{w}_p) - \check{\mathbf{s}}(t))^2 dt, \quad (43)$$

with $\mathbf{s}(t) = [x(t), z(t)]$ the drone position at time t .

5.3. Thermal Management of Cryogenic Storage

Test case description and control problem. We consider the thermal management of a cryogenic tank. This is a fundamental challenge in long-duration space missions, which require storing large amounts of cryogenic propellant for long periods. These fluids must be stored in the liquid phase to maximize the volumetric energy density. However, their storage temperatures are extremely low (e.g., -250 °C for liquid hydrogen), and their latent heat of evaporation is much smaller than that of non-cryogenic propellants. These combined factors challenge the storage because evaporation due to thermal loads produces a continuous pressure rise over time (Salzman, 1996; Motil et al., 2007; Chai and Wilhite, 2014).

The efficient management of this problem requires a combination of advanced insulation strategies (see Mer et al. 2016b; Jiang et al. 2021) and venting control strategies (Lin et al., 1991). In this test case, we consider a classic active Thermodynamic Venting System (TVS), similar to the one presented in Lin et al. (1991) and recently characterized in Imai et al. (2020); Qin et al. (2021). Figure 8a shows the schematics of the TVS configuration.

We consider a tank of volume V_t filled with a volume of liquid $V_l(t)$, operating at a nominal pressure p_0 while subject to a time-varying heat load $Q_h(t)$. The TVS is composed of a vented branch and an injection loop. In the vented branch (blue line in Fig.8a), a mass flow rate \dot{m}_c is extracted from the tank, expanded through a Joule-Thomson valve (1) and used as a cold source in a heat exchanger (2) before being expelled. In the injection loop, a mass flow rate \dot{m}_h is circulated by a pump (3) into the hot side of the heat exchanger and reinjected into the tank as a subcooled liquid. This injection can be carried out via a submerged jet or a spray bar (Hastings et al., 2005; Wang et al., 2017; Hastings et al., 2003), but this distinction is unnecessary for the illustrative purposes of this work. An extensive literature review of TVS approaches is presented by Barsi (2011), who also introduced and tested two simplified approaches for the thermodynamic modelling of the problem (see Barsi and Kassemi 2013a and Barsi and Kassemi 2013b). Figure 8b maps the (ideal) key state of the fluids at the inlet and outlet of each component in the $T - s$ (temperature vs. specific entropy) diagram. The state of the liquid and the vapour in the tank are denoted with subscripts (l) and (v) , the states (1) and (2) are the inlet and outlet of the heat exchanger on the vented line, while states $(1')$ and $(2')$ are their counterparts on the injection side.

The control task is to keep the tank pressure below the maximum admissible one while venting the least amount of liquid. The simplest control problem, and also the one implemented in this work, consists of

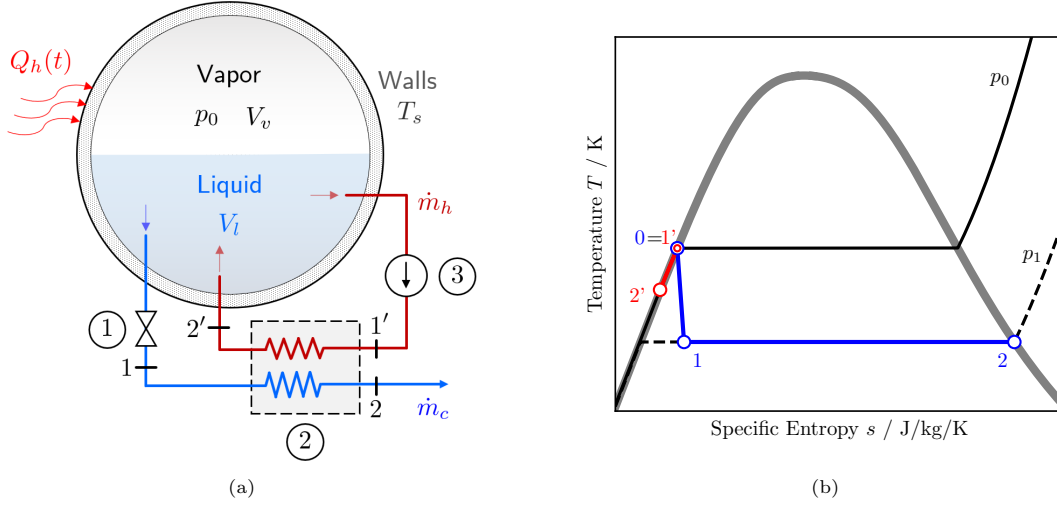


Figure 8: Schematic of the thermal management problem considered in this work. A cryogenic tank of volume V_t , containing a volume V_l of saturated liquid and $V_t - V_l$ saturated vapour, is subject to a heat load $Qh(t)$. The figure on the right traces the state of the system on the temperature-specific entropy diagram considering the simplified model used to simulate the environment.

employing the pressure difference $\Delta p_V = p_0 - p_1$ as the sole control parameter. The Δp_V is linked to the mass flow rates in the J-T valve (1) and the pump (3) by limiting the operating range of the heat exchanger and by imposing that only latent heat is to be recovered from the venting line. Therefore, defining as $\Delta T_l(p_1) = T_l - T_l(p_1)$ the temperature drop produced by the J-T device and $\Delta h_c(p_1) = h_2 - h_1 = h_{v,\text{sat}}(p_1) - h_{l,\text{sat}}(p_0)$ the specific latent heat remaining on the vented line, one has

$$\dot{m}_h(p_1) = \frac{\Delta h_c(p_1)}{c_{p,l} \Delta T_l(p_1)} \dot{m}_c(p_1). \quad (44)$$

Furthermore, to limit the control action exclusively to Δp_V , we assume that the pump (3) is equipped with flow regulation to follow (44) and we link the vented flow rate \dot{m}_c to Δp_V and the J-T valve's characteristic through

$$\dot{m}_c(\Delta p_v) = \sqrt{\Delta p_v / K_{JT}}, \quad (45)$$

with K_{JT} the valve's pressure drop constant. Considering the maximum pressure drop along the JT-valve Δp_{max} , the desired operational pressure \tilde{p} and defining $e(t) = p(t) - \tilde{p}$ the tracking error, we consider a simple policy parametrization of the form

$$\Delta p_V = a(e, \mathbf{w}_a) = \frac{1}{2} \Delta p_{\text{max}} (\tanh(w_{a1}e + w_{a2}e^3 + w_{a3}) + 1). \quad (46)$$

We treat Δp_{max} as a pre-defined constant and use $\mathbf{w}_a = [w_{a1}, w_{a2}, w_{a3}]$ as policy parameters. w_{a3} acts as an offset in the policy, controlling the threshold pressure above which the valve opens, while w_{a1} controls the slope of the hyperbolic tangent, i.e. the sensitivity of the policy to the tracking error. The cost function driving the model-based controller and the model-free agent are

$$\mathcal{J}_a = \frac{1}{T_o} \int_0^{T_o} \alpha_1 e^2(t) + \alpha_2 \dot{m}_c dt \quad \text{and} \quad \mathcal{R}_c = -\frac{1}{n_t} \sum_0^{n_t-1} \alpha_1 e(t_k)^2 + \alpha_2 \dot{m}_c(t_k), \quad (47)$$

with the $\alpha_1, \alpha_2 \in \mathbb{R}$ used to non-dimensionalize the inputs and weight the penalty on the mass consumption versus the primary objective of keeping the pressure constant.

To set up the data-driven identification to this control law, we assume that the tank is instrumented with a pressure sensor sampling $\tilde{p}(t)$ and a flow rate sensor on the vented line to measure $\tilde{m}_v(t)$.

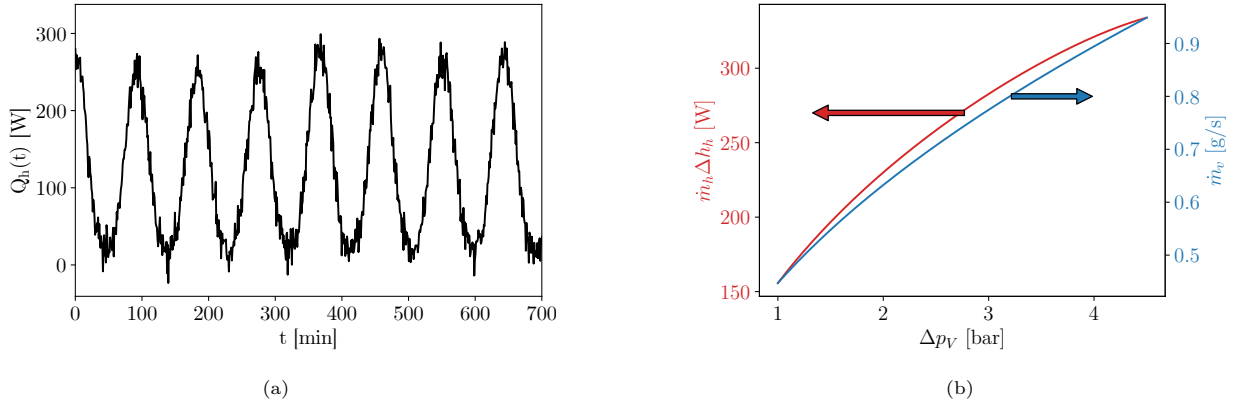


Figure 9: Sample profile of the thermal load (exogenous input) considered in test case 2 (Fig a) and impact of the control parameter (p_1) on the vented flow rate and subcooling of the injection line.

Selected conditions and environment simulator. We consider a cryogenic tank with volume $V_t = 60 \text{ m}^3$ with a desired operational pressure $\tilde{p} = 500 \text{ kPa}$ filled with liquid hydrogen. At the start of each episode, the tank is 70% full and pressurized to an initial value sampled from a normal distribution with mean $\bar{p}_0 = 500 \text{ kPa}$ and standard deviation $\sigma_{p_0} = 25 \text{ kPa}$. The thermal load applied to the tank fluctuates from a minimum of roughly 50 W to a maximum of 300 W with a period of $T_h \approx 1.5 \text{ h}$. This cyclic load mimics the large thermal fluctuations a tank could face in orbit as it is periodically exposed to direct sun radiation. The chosen period is approximately the time it takes the International Space Station (ISS) to complete an orbit around Earth. The load profile is shown in Figure 9a. This load is constructed as a pseudo-random signal made of Gaussian-like peaks randomly varying within $[0.9, 1.1]$ times the nominal peak, lifted by the minimal load and polluted by uniform noise with a standard deviation equal to 10% the nominal peak.

The simulation of the real environment and the digital twin are carried out using the same simplified model. In particular, we employ the homogeneous model presented in Barsi (2011), adapted to account for the venting line similarly to Mer et al. (2016a). This approach assumes that the liquid and the vapour are in saturation conditions. This is an oversimplification because usually the liquid is subcooled, and the vapour is superheated. We consider two control volumes: the saturated mixture and the solid wall. We refer to Marques et al. (2023) and Barsi and Kassemi (2013b) for more advanced models and to Panzarella and Kassemi (2003) and Panzarella et al. (2004) for an in-depth discussion on the limits of thermodynamic models. Focusing only on the storage problem (no out-flow except venting), the conservation of internal energy of the solid, and the mass and enthalpy of the saturated mixture read

$$\frac{d}{dt} [m_s c_s T_s] = Q_h(t) - Q_{s \rightarrow f}, \quad (48a)$$

$$\frac{d}{dt} [\rho_v (V_t - V_l(t)) + \rho_l V_l(t)] = -\dot{m}_c, \quad (48b)$$

$$\frac{d}{dt} [\rho_v h_v (V_t - V_l(t)) + \rho_l h_l V_l(t)] = Q_{s \rightarrow f} + V_t \frac{dp}{dt} - \dot{m}_c h_l + \dot{m}_h \Delta h_h, \quad (48c)$$

where ρ is the density, h is the specific enthalpy, and $\Delta h_h = h_{2'} - h_{1'}$ is the variation of specific enthalpy on the injection loop provided by the heat exchanger. All properties are at saturation conditions, and the subscripts l and v refer to the liquid and the vapour phases, respectively. We consider the mass m_s and specific heat capacity c_s of the wall to be constant. Denoting as $H = \rho h$ the (volumetric) enthalpies and using the chain rule to have $d(\cdot)/dt = (d(\cdot)/dp) (dp/dt)$, these can be written as

$$m_s c_s \frac{dT_s}{dt} = Q_h(t) - Q_{s \rightarrow f}, \quad (49a)$$

$$\frac{dV_l}{dt} = \frac{1}{(\rho_l - \rho_v)} \left[\left(\frac{d\rho_v}{dp} - \frac{d\rho_l}{dp} \right) \frac{dp}{dt} V_l(t) - \dot{m}_c - \left(\frac{d\rho_v}{dp} \right) \frac{dp}{dt} V_t \right], \quad (49b)$$

$$\frac{dp}{dt} \left\{ \left(\frac{dH_l}{dp} - \frac{dH_v}{dp} \right) V_l(t) + \left(\frac{dH_v}{dp} - 1 \right) V_t \right\} = \left(H_g - H_l \right) \frac{dV_l}{dt} + Q_{s \rightarrow f} - \dot{m}_c h_l + \dot{m}_h \Delta h_h. \quad (49c)$$

The heat transferred from the wall to the fluid mixture is modelled using Newton's cooling law $Q_{s \rightarrow f} = U_s(T_s - T)$, where U_s is the overall heat transfer coefficient. Taking all liquid and vapour properties from thermophysical property libraries, this is a closed set of implicit differential equations for $\mathbf{s} = [T_s, V_l, p]$. The fluid properties are retrieved through the open-source library CoolProp (Lemmon et al., 2018), which is based on multiparameter Helmholtz-energy-explicit-type formulations and also provides accurate derivatives.

For a given design of the evaporator, one can link the subcooling in the injection line (term $\dot{m}_h \Delta h_h$ in (48c)) to p_1 using standard methods for heat exchanger design (see Cengel and Ghajar 2019). This can be written as $\dot{m}_h \Delta h_h = \varepsilon c_{p,l} \Delta T(p_1)$, with $\varepsilon = 1 - e^{-NTU}$ the efficiency of the heat exchanger, $NTU = U_{HX} A / (\dot{m}_h c_p)$ the number of transfer units and U_{HX} the overall heat transfer coefficient. For the sake of this problem, we assume that the heat exchanger is a shell-and-tube design with 200 tubes of $D = 5$ mm diameter and $L = 2$ m length, for a total exchange area of $A = 6.2$ m². Taking a wall/fluid heat transfer coefficient of $U_s = 50$ W/(m²K), a global heat transfer coefficient of $U_{HX} = 75$ W/(m²K) and a valve with $K_{JT} = 500$ GPa·s²/kg² gives the thermal power exchange and the vented flow rate in Figure 9b.

Model predictions are thus possible once these three parameters are provided. We consider these the model closure for the digital twin, hence $\mathbf{w}_p = [U_s, U_{HX}, K_{JT}]$. These are to be inferred from real-time data by minimizing the following cost function.

$$\mathcal{J}_p = \frac{1}{T_o} \int_0^{T_o} \alpha_3 (\tilde{T}_s(t) - T_s(t))^2 + \alpha_4 (\tilde{V}_l(t) - V_l(t))^2 + \alpha_5 (\tilde{p}_l(t) - p_l(t))^2 dt, \quad (50)$$

where the parameters $\alpha_3, \alpha_4, \alpha_5 \in \mathbb{R}$ are used to give comparable weight to these terms despite the largely different numerical values. To simplify the calibration of this digital twin model, in addition to the pressure sensor, we assume that a liquid level indicator is available, allowing for monitoring the liquid level $\tilde{V}_l(t)$, as well as temperature sensors to acquire $\tilde{T}_s(t)$.

6. Results

This section presents the performances of the RT algorithm in controlling and assimilating a wind turbine subject to time-varying wind speed (T1, 5.1), a flapping wing micro air vehicle (FWMAV) against head wind (T2, 5.2) and a cryogenic tank exposed to fluctuating thermal load (T3, 5.3). The hyper-parameters selected for each test case and the respective simulation configurations are listed in Table 1. We use five different random seeds for our simulations to extract performance statistics across different initial states of the optimizers. For both T1 and T2 we take the gradients ensemble over $N_z = 5$ realizations, whereas in T3 we considered $N_z = 1$, for the overall limited level of noise in the exogenous disturbance. In all studies, the first policy to be deployed onto the real system is the model-free one. Finally, for all test cases, we set $n_S = 1$, as detailed in Section 4.3.

Table 1: RMA Experiments: test cases configurations and hyper parameters settings.

	T_o (s)	dt (s)	n_e	N_z	n_Q	n_A	n_G	n_{mb}	P_π	P_w	T_J	T_w
T1 (Sec. 5.1)	600	$5 \cdot 10^{-1}$	20	5	500	1000	15	10	2	3	1	0.5
T2 (Sec. 5.2)	5	$5.0 \cdot 10^{-4}$	20	5	1000	1000	15	5	4	4	1	0.5
T3 (Sec. 5.3)	$4.32 \cdot 10^5$	30	20	1	1000	1000	30	5	4	20	1	0.5

6.1. Learning Performances

The learning performances for all the three cases are reported in Figure 10 and their numerical values tabulated in Table 2. The Figure shows the mean control or assimilation performances (first or second column, respectively) as a dashed line, and their relative standard deviation as a shaded area. The joined model-based and model-free control paradigm learns how to control effectively the system in a limited number of iterations for all test cases, showing good sample complexity. Indeed, the average control performance (\mathcal{L}_a) is in the order of $\mathcal{O}(10^{-1})$ with respect to the initial condition, performing thus up to ten times better the initial policy. The high standard deviation at the beginning of the training is associated with the initial exploration phase of the model-free side, and it consistently decreases with the iterations, as it converges to a specific region of the search space, as shown in Figures 10c and 10d whereas in Figure 10a it is roughly constant. Analysing the adjoint-based assimilation performances, Figures 10b, 10d and 10f show that the methodology is able to tailor the digital twin on the current system specifics in five to ten iterations. At the end of the training process, it obtains an \mathcal{L}_p of $\mathcal{O}(10^{-1})$, $\mathcal{O}(10^{-2})$ and $\mathcal{O}(10^{-4})$, normalized with the performances of the initial guesses of \mathbf{w}_p , for T1, T2 and T3, respectively. This, in turn, reflects on the model-based policy optimization (Step 5). In fact, as the digital twin predicts with greater precision the dynamics of the system for different actuations also the quality of the policy optimized “offline” increases. This also affects the policy switch (Step 6), as it becomes more accurate in choosing the best policy to be deployed on the real system. The effect of Step 6 is illustrated in Fig. 11.

Table 2: RMA Learning performances, normalized by the mean initial cost.

	$\mathcal{L}(\mathbf{w}_p^*)/\mathcal{L}(\mathbf{w}_p^0)$	$\mathcal{L}(\mathbf{w}_{a,mb}^*)/\mathcal{L}(\mathbf{w}_{a,mb}^0)$	$\mathcal{L}(\mathbf{w}_{a,mf}^*)/\mathcal{L}(\mathbf{w}_{a,mf}^0)$
T1 (Sec. 5.1)	$(2.1 \pm 0.8) \cdot 10^{-1}$	$(0.8 \pm 0.5) \cdot 10^{-1}$	$(1.3 \pm 1.2) \cdot 10^{-1}$
T2 (Sec. 5.2)	$(3.2 \pm 4.9) \cdot 10^{-2}$	$(4.18 \pm 0.01) \cdot 10^{-1}$	$(2.01 \pm 0.45) \cdot 10^{-1}$
T3 (Sec. 5.3)	$(3.15 \pm 0.9) \cdot 10^{-4}$	$(4.47 \pm 2.68) \cdot 10^{-1}$	$(4.80 \pm 3.15) \cdot 10^{-1}$

All experiments begin with the model-free policy driving the interactions with the real environment, i.e. as “live policy”, while the model-based is initially set as “idle”. Then, if the model-based performs better for P_π iterations, it takes over as “live” policy following the decision tree of Step 6, illustrated in Figure 3. This is what happens at $n_e = 7$ in T1, and $n_e = 4$ for both T2 and T3. When this happens, the two paradigms, model-based and model-free, start to interact, as shown in Figure 11 especially appreciable in Figures 11a and 11c. We observed that as soon as the model-based takes the lead of the interactions with the real system the model-free control performance registers a steeper improvement. Arguably, this has two causes: (1) the model-based acts as an “expert” for the model-free, providing high quality samples recorded in $\mathcal{D}_\mathcal{L}$ from which the model-free loop can learn; and (2) the critic gets better at predicting the value associated to the recorded transitions. Interestingly, in both T1 and T3 (Figure 11a, 11c), the model-free learns a better policy imitating the model-based counterpart, effectively “surpassing the master” and being selected to be the “live” policy again. Comparing the performances of the model-based and model-free loops, In T1 the model based performs slightly better, in T2 the model-free performs roughly 50% better than the model-based and in T3 they converge to the same policy, thus we could not conclude about the general performance of the model-based and model-free policy optimization loops.

6.2. Wind turbine Control

The digital twin performances, parametrized by the best set of weights \mathbf{w}_p^* , are shown in Figure 12. Figure 12a shows the average prediction versus the average system evolution as a function of time, while Figure 12b in the middle plots one versus the other. We conclude that the digital twin successfully tracks the dynamics of the real system. However, it shows a systematic under-estimation of roughly $\Delta \mathbf{s} \lesssim 1$ (rad / s) or 9.55 (RPM), especially localized at low rotational speeds. Whether this bias is inherently linked with the chosen parametrization or an insufficient number of samples requires further investigation. It is worth of notice that, while in T2 and T3 the coefficients to be identified represent the “ground truth”, in this test case there is not such a baseline, as the initial coefficients \mathbf{w}_p^0 , derived in the work of Saint-Drenan et al. (2020), describe a power curve in steady wind conditions. As a consequence, the RT algorithm optimizes

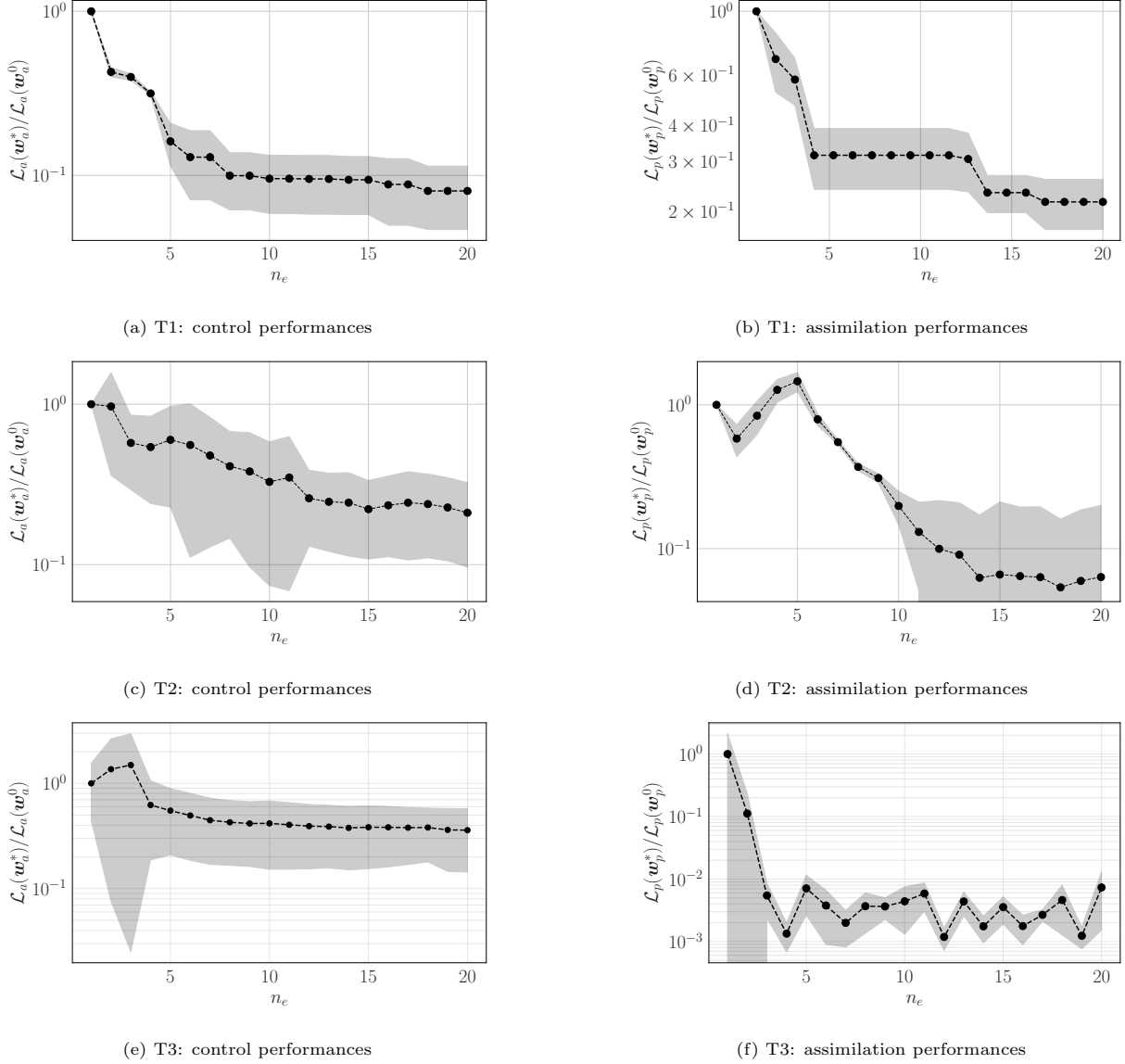


Figure 10: Control $\mathcal{L}_a(\mathbf{w}_a)$, and assimilation performances, $\mathcal{L}_p(\mathbf{w}_p)$. Both are normalized by the initial cost, $\mathcal{L}_a(\mathbf{w}_a^0)$ and $\mathcal{L}_p(\mathbf{w}_p^0)$, respectively.

them to adapt to the dynamic a time-varying wind field as the system progresses. Therefore, the average assimilator loss $\mathcal{L}_p \approx \mathcal{O}(10^{-1})$ highlights the capability of the algorithm to adapt online, possibly taking into consideration changes in the operative conditions of the system itself, i.e. blade erosion and relative decrease in aerodynamic performances.

The control performances are summarized in Figure 13. The controller is able to keep the system close to the desired set-points, Figures 13a and 13b. This is especially true for what concerns the power, always kept very close to \bar{P} , even in noticeably varying wind speeds (Figure 13b). On the other hand, it consistently keeps the generator speed, ω_g , below-rated conditions, of approximately $\Delta s \approx 8$ rad/s. This lower-than-rated rotational speed reflects on the actuated torque, Figure 13d, which is always in the middle between the allowed action space. In addition, the very fast actuation rate on the torque, $\dot{\tau} = 15$ kN, allows the controller to rapidly adapt in case of abrupt change in the wind speed, while fine tuning the actuation with

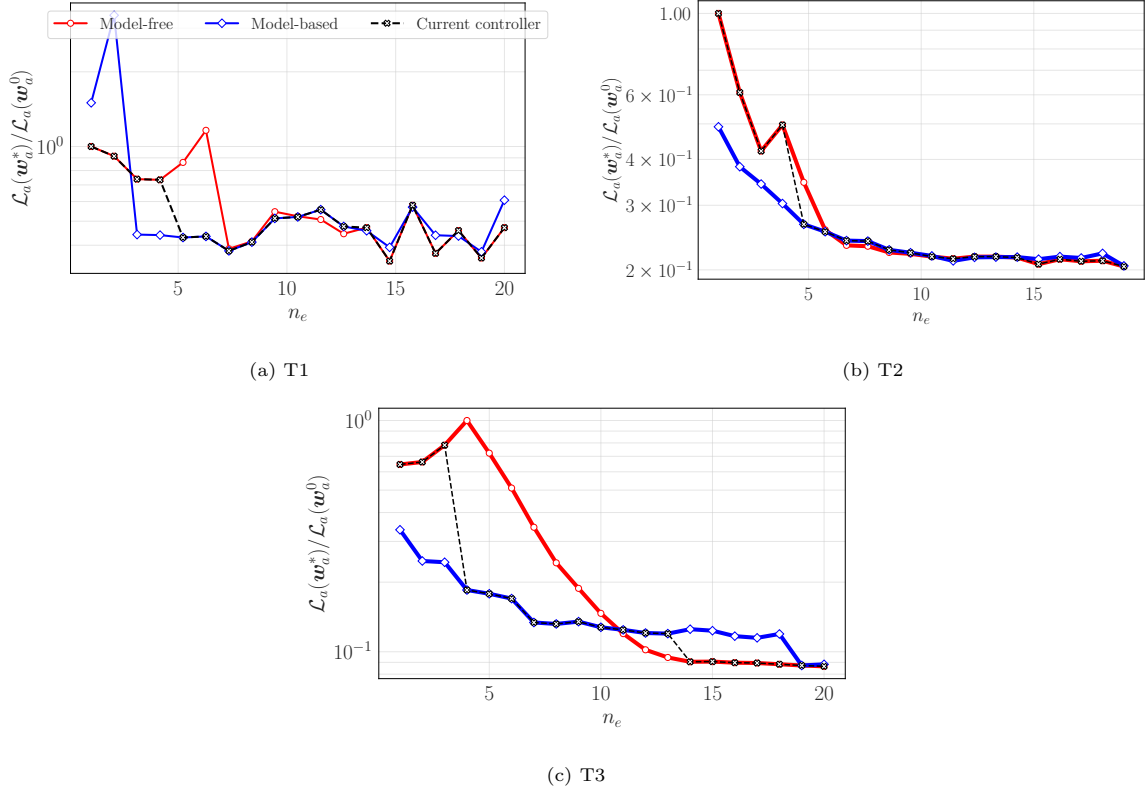


Figure 11: Policy switch detail. Switch between “live” and “idle” policies, during interactions with real system.

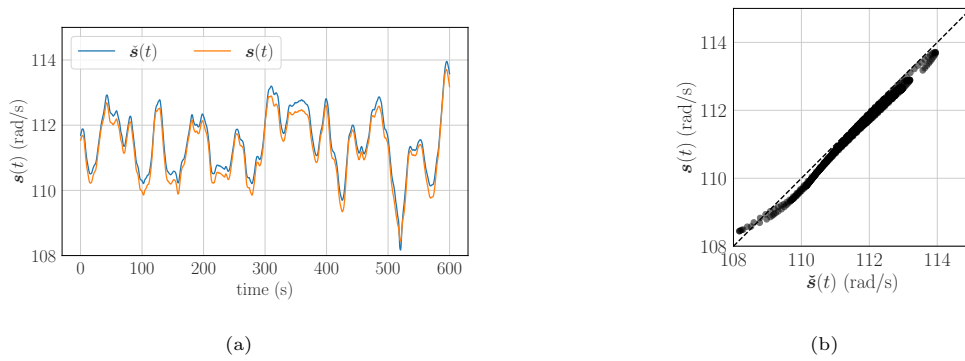


Figure 12: Digital Twin agreement with real system. Evaluation of the optimal $\mathbf{w}_p = \mathbf{w}_p^*$ with randomized initial conditions and disturbances. Time-series (a) and scatter plot (b), plotting real state on the x-axis and predicted one on the y-axis.

the pitch angle, β . The latter follows consistently the wind speed, which is desirable. At higher wind speeds than rated, i.e. $u_\infty > 11.4$ m/s, it consistently plays on the blades' angle to reduce the aerodynamic torque to keep the system close to desired conditions. We note that this lower-than-rated ω_g strategy be mitigated, if desired, tuning the normalization coefficients α_1 and α_2 , possibly increasing the penalty commonly done in multi-objective optimization problems.

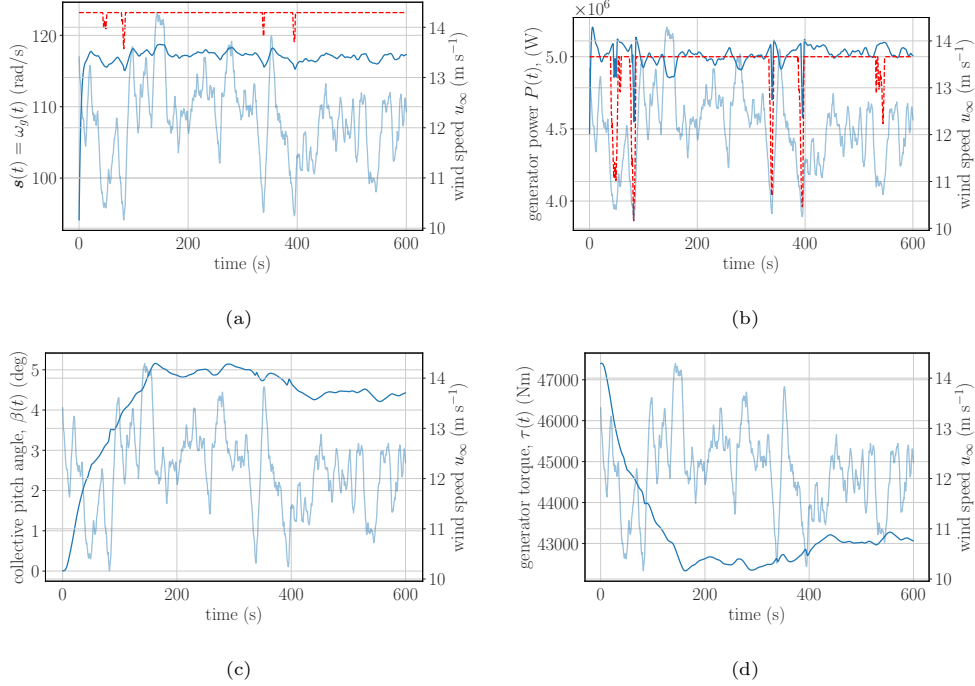


Figure 13: Control performances. System evolution against set-points (dashed red line) in (a) and (b), filtered actuations in (c) and (d).

This decrease in C_p is better appreciated in Figure 15b, which shows the power coefficient trend against wind speed. This shows a peak, at rated conditions $u_\infty \approx 11$ (m/s) with a $C_p = 0.42$, steadily decreasing for higher winds, as expected in common wind turbine control strategies.

The model-based and model-free policies are compared in Figure 15. The two optimization loops converge to essentially the same parametrizations, leading to the same policy functions, as also supported by the very similar mean cost functional \mathcal{L}_a listed in Table 2. The only (minor) difference appearing to be the threshold

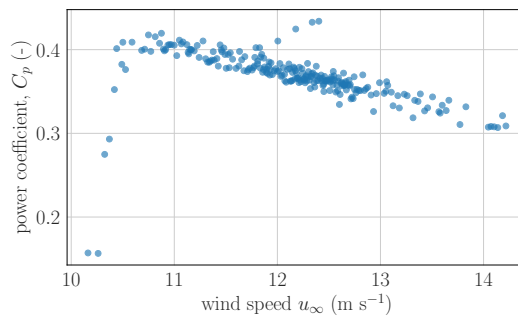


Figure 14: Reduction of the power coefficient C_p against wind speeds.

in the actuation of the torque. In both cases, when the error goes on the rotational speed goes negative, i.e. $e_i = \omega_g - \tilde{\omega}_g < 0$, the controllers reduce the pitch angle (Figures 15a,15c) to increase the aerodynamic efficiency and, consequently, the harvested aerodynamic torque, with the goal of increase the rotational speed to get closer to the set point. The opposite is true when the generator is spinning too fast: the controller increases the angle of attack of the blades to slow the generator down. The integral of the error over the past revolution, $\int e$, essentially decides on the slopes of the control surface. Interestingly, looking at the torque actuation shown in Figures 15b, 15d, it seems that this control actuation is almost insensitive to this control input, relying on the scalar error solely. This control surface is directly connected with the objective of keeping the power around the rated value of $P = 5MW$. In fact, as the error becomes negative, the controller increases the torque, to keep the power at the end of the generator constant ($P_g = \omega_g \cdot \tau_g$). On the other hand, when the error increases, it reduces the resistive torque, relying on the pitch actuator to reduce the speed while keeping the power constant.

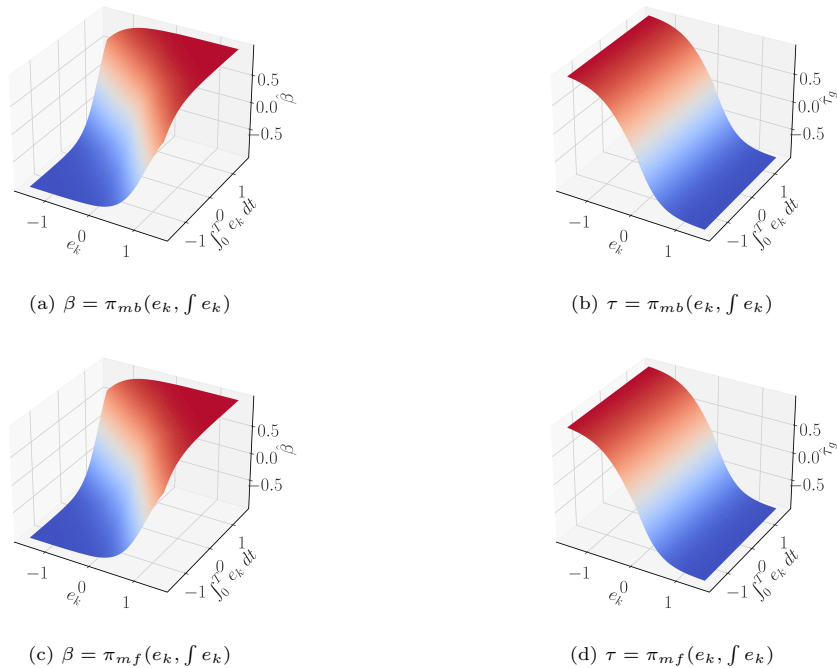


Figure 15: Normalized policy contours, for the model-based (firsts two) and model-free (following) actor. As a function of the error $e_k(t) = \omega_g(t) - \tilde{\omega}_g(t)$ and its integral over the past revolution.

Lastly, we conclude this analysis investigating the robustness of the found models, shown in Figure 16. Specifically, we run one-hundred simulations, on randomized initial conditions and sampled disturbances, possibly unseen during the training phase, using the found policies parametrizations $\mathbf{w}_{a,mb}^*$, $\mathbf{w}_{a,mf}^*$ and assimilation parameters \mathbf{w}_p^* . The control performances, Figure 16a show a multi-modal distribution. The stronger peak is located in a good performance region, close to $L_a \lesssim \mathcal{O}(10^2)$. This supports the good performances shown above. However, it appears that the model is not able to extrapolate the control strategies in unseen conditions outside of a given “confidence” region. This may be due to several factors. A first hypothesis is that it could be beneficial to use more wind fields time series (and relative realizations) to get a broader picture of the possible operative conditions, possibly increasing their diversity, or considering an higher number of realizations N_z . Another way of possible improvement may lie in the function approximators used for the policy function, currently just a linear combination of the inputs, which could possibly increase the descriptive capabilities of the model. Nevertheless, we considering the control task successfully achieved for the nominal operative conditions and leave these investigations for future works more centred

on wind turbines control. The assimilations performances, on the other hand, are reliably on-track with respect what experienced during the learning phase. The digital twin tracks the real system with very small deviation, $\mathcal{L}_p < \mathcal{O}(0.5 \cdot 10^5)$ for most situations. However, this model may also be improved to take into account both the minor bias presented in Figure 12 and to be more flexible in adapting to new conditions.

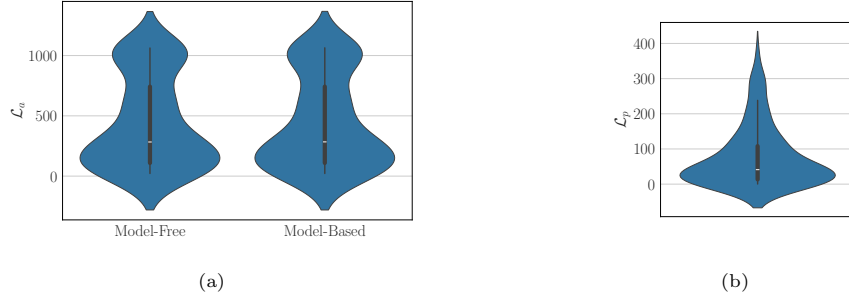


Figure 16: Robustness analysis of the control policies (a) and assimilated model (b)

6.3. Trajectory control of flapping wings micro air vehicles

In this test case, the initial weights $\mathbf{w}_p^0 = [a, b, c]$, pertaining the lift and drag closure (equation (41) and (42)), are drawn from three random distributions, and a stopping criterion was defined to interrupt the n_G iterations if the cost falls below a given threshold (10^{-2}). Figure 17a shows the assimilation performance of the digital twin in predicting the real-system behavior. The two show a small deviation. This can be better appreciated in Figure 17b, which shows that the states predicted by the digital twin (y-coordinates) corresponds with good agreement with the true states (x-coordinate) experienced by the real environment, thus lying on the diagonal of the plot.

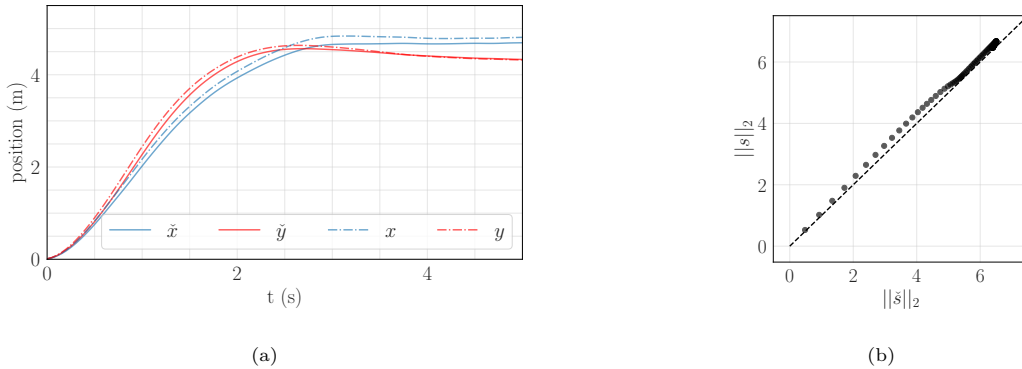


Figure 17: Comparison of the time evolution of the drone position for the real environment (solid lines) and the digital twin (dashed line). The right plot shows the high correlation between the norm of the predicted state $\mathbf{s} = [\hat{x}, \hat{y}, x, y]$ and the real state \mathbf{s} for an episode length.

The training detailed in Section 6.1 converges to one optimal policy that the drone applies to control its flight in the real environment. Figure 18 characterizes one such flight depicting the state variables (18a and 18b) and the control actions (18c). The figures evidence that the drone managed to closely reach its target ($\mathbf{x}_f = 5$ m and $\dot{\mathbf{x}}_f = 0$, as fast as possible) thanks to the control of the stroke plane angle β_w and the flapping amplitude A_ϕ . The control of the latter is mainly formed of three phases in a kind of bang-bang fashion. First, the drone flaps its wings at their maximum angle of attack ($A_\phi = 88$ deg) to reach the target position as fast as possible. Then, the drone picks a flapping angle close to the minimal one (55 deg) to

decelerate and stabilize at the target height with minimal overshoot. Finally, the wings flap at a slightly bigger angle so that they generate enough lift to balance the body weight. The lift is also slightly modulated by the other control variable (β_w) which mainly drives the horizontal motion of the drone. At the start of the episode, the drone pitches the stroke plane up to the maximum angle ($\beta_w = -30$ deg) and then stabilizes it around an angle that allows it to stay close to the desired position, x_f , despite the headwind. The influence of the gust is visible on β_w even though the wind effect is still very limited, due to the selected mass and surface of the body.

Figure 19 analyses the policies found by the model-free (Figures 19a - 19d) and model-based (Figures 19e - 19h) loops. To this end, we fix two of the four inputs to zero and span on the other two dimensions, recording the corresponding action. The two policies are remarkably similar, converging to essentially the same parametrization with their differences lying in the concavity of the hyperbolic tangent, as dictated by the biases. This affects the localization of the switching between the two bounds of the actuation space, possibly explaining the differences in their associated costs presented in Table 2. In both cases, for what concerns \hat{A}_ϕ , the demarcation zone between the two bounds lies on the diagonal that goes from $(\hat{e}_x, \hat{e}_x) = (-1.0, -1.0)$ to $(\hat{e}_x, \hat{e}_x) = (0.25, 1.0)$, see Figure 19a. The same trend is observed in Figure 19b, which analyses the dependencies from e_z and its time derivative. In this case, however, the upper point of the diagonal lies around $(\hat{e}_z, \hat{e}_z) = (0.0, 1.0)$, thus increasing \hat{A}_ϕ as the rate of change of e_z goes negative, and decreasing it otherwise. Interestingly, the model-based policy here shows a broader decision zone, as depicted in Figure 10f. Now, analysing the actuation on β_w , the threshold appears to be positioned in the diagonals $(\hat{e}_x, \hat{e}_x) = (0.0, -1.0)$ to $(\hat{e}_x, \hat{e}_x) = (0.75, 1.0)$. The sensitivity to the z -errors instead show it to lie in $(\hat{e}_z, \hat{e}_z) = (-1.0, 0.0)$ and $(\hat{e}_z, \hat{e}_z) = (1, 0.5)$. Therefore, it seems that the time variation of the rate of change is the most important input on the x -dimension, whereas in the z -coordinate, it is the scalar \hat{e}_z . Arguably this may be caused by the headwind, oriented as opposite of the x -versor. Overall, there appears to be two main mechanisms at play: (1) the errors and their rate of change seems to have the same importance when deciding how to control on \hat{A}_ϕ being slightly more sensitive to the scalar instantaneous errors; and (2) when deciding on how to actuate β_w , the controller balances the scalar instantaneous error in one dimension and its rate of change in the other. In fact, when \dot{e}_x increases, it actuates on β_w to get back to nominal conditions, and the same is observed on analysing the reactivity to the instantaneous error e_z and e_x .

We conclude the FWMAV analysis presenting the robustness study of the model-free and model-based policies, shown in Figure 20. One-hundred episodes were run on the real environment for each policy and their costs are compared with violins plots (Figure 20a). Both sets of weights result in a small cost proving their capability to handle the random gust. The model-free policy manages to reach on average a lower cost and shows a slightly different distribution than the model-based policy, having two peaks at $\mathcal{L}_a = 905$ and $\mathcal{L}_a = 920$, whereas the model-based shows a main peak in the middle, at $\mathcal{L}_a = 910$. However, their differences are in the order $\mathcal{O}(10^1)$, reinforcing the observation that the two have converged to a very similar policy. Lastly, The same procedure is then applied on the assimilation side, studying its robustness to varying operative conditions, as shown in Figure 20b. It appears that the identified closure function is robust to different operative conditions, registering a mean cost of $\mathcal{L}_p \approx \mathcal{O}(10^{-3})$.

6.4. Thermal management of cryogenic storage

At last, we examine the RT results on the cryogenic thermal management test case. The digital twin assimilation consists of identifying the weights $\mathbf{w}_p = [U_s, U_{HX}, K_{JT}]$ which drive the heat transfer between the cryogenic tank and the environment, as well as the performance of the active TVS. For all simulations, this vector was initialized taking $\mathbf{w}_p^0 = [1, 1, 10]$, with the units of the first two components being (W/m²K), and the last being (GPa·s²/kg²).

The agreement between the predicted state and the real one is presented in Figure 21, which shows both the time series of the real and predicted states (Figures 21a - 21c) and their direct comparison plotting one against the other (Figures 21d - 21f). All three components are successfully identified, even though slight deviations are found for $\mathbf{s}_1 = p$ and $\mathbf{s}_2 = T_s$.

The control performances of the optimal parametrization, \mathbf{w}_a^* , extracted from the learning curve presented in Figure 10d are studied next. The current scenario involves an initial over-pressurized tank operating

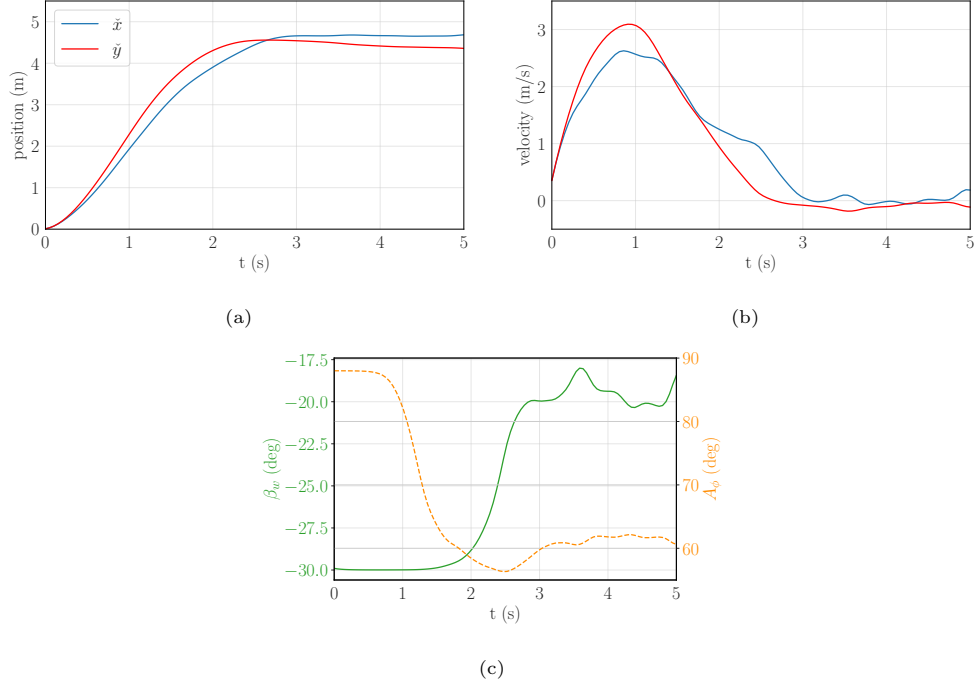


Figure 18: Time evolution of the positions x and y (a) and the velocities \dot{x} and \dot{y} (b) of the flapping wing micro air vehicle driven by the control actions $\mathbf{a} = [A_\phi, \beta_w]$ (c). The optimal control policy manages to lead the drone to its target $(x, y) = (5, 5)$ and $(\dot{x}, \dot{y}) = (0, 0)$ within one episode time with minor oscillations that results from the gust.

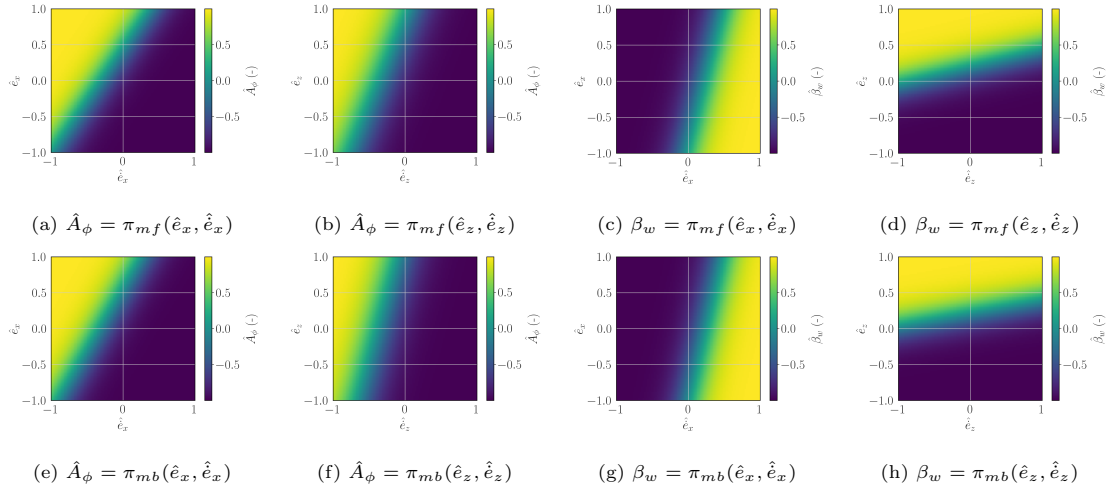


Figure 19: Comparison of model-based and model-free policies

0.4 bar above the reference \tilde{p} . Figure 22 shows the time evolution of the real pressure \tilde{p} and propellant mass \tilde{m}_l over time, while the vented mass flow rate \tilde{m}_c . Figures 22b and 22c show the control action over time and the corresponding pressure, respectively. Since the tank is initially in an over-pressurized state sufficiently far from \tilde{p} , the valve was regulated to open to at its widest ($\dot{m}_c = 0.63$ g/s) allowing the pressure to rapidly reduce until the target 5 bar are reached. This pressure drop is accompanied by a consumption of 87 kg over two roughly 45 hours. Once the target is reached, the active TVS regulates the pressure around this value. To do so, \tilde{m}_c fluctuates between -50% and 25% around its midpoint due to changes in the heat due

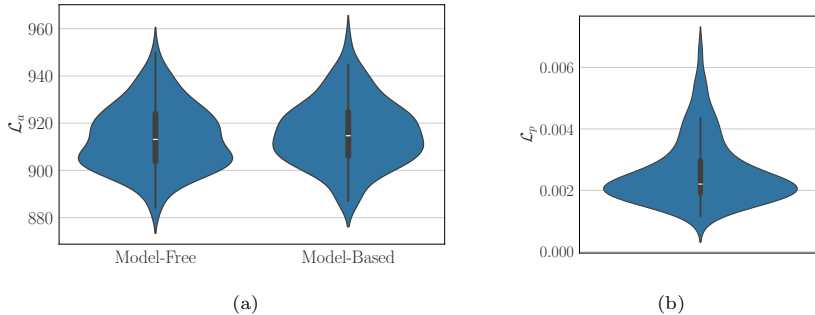


Figure 20: Violin plots of the model-free and model-based policies compute over 100 episodes. Both policies result in similar distributions with a lower average cost for the model-free policy

to the disturbance, although such variations are not seen in the pressure signal.

From these findings, we conclude that the control policy is able to completely control the tank pressure around its desired target value. However, the response time of the TVS is limited by the technical constraints assigned to the circulating pump, and Joule-Thomson valve. In addition, depending on the value assigned to the K_1 constant in 47, one could retrieve either faster or more fuel-efficient policies.

We inspect the two found policies in Figure 23. The two loops, model-based and model-free, converge to essentially the same parametrization. They show almost identical response to the possible input space, with very minor discrepancies in the inclination of the hyperbolic tangent. Lastly, the robustness of the assimilation and control loops concludes this overview. The procedure consists in evaluating the cost of the optimal weights w_p and w_a over observations unseen during the training phase. To this end, we carried out one-hundred simulations on random initial conditions and disturbances. For each of them, we computed the assimilation cost \mathcal{L}_p , as well as the control cost \mathcal{L}_a using the model-based and model-free policies. This investigation, summarized in the violin plots presented in Figures 24a and 24b, proves that the weights obtained at the end of the learning phase are valid and robust even in unseen scenarios. Moreover, in contrast to what was observed in the wind turbine test case, the model-based and model-free weights are nearly identical, thus their performances are also identical as supported by Table 2 which shows a difference between the two control performances in the order of $\mathcal{O}(10^{-2})$. This is likely a consequence of both approaches converging in the same region of the search space.

7. Conclusions and outlooks

We presented a novel framework to train physics-based digital twins from real-time data while at the same time training a control agent through a combination of model-free and model-based methods. We called this framework Reinforcement Twinning (RT), and we positioned it at the intersection between data assimilation, system identification and reinforcement learning. The digital twins are formulated as physics-based models relying on closure laws expressed as parametric functions. The parameters defining these closures are identified from real-time data using an adjoint-based data assimilation strategy.

We presented a novel framework to train physics-based digital twins from real-time data while at the same time training a control agent through a combination of model-free and model-based methods. We called this framework Reinforcement Twinning (RT) and positioned it at the intersection between data assimilation, system identification and reinforcement learning. The digital twins are formulated as physics-based models relying on closure laws expressed as parametric functions. The parameters defining these closures are identified from real-time data using an adjoint-based data assimilation strategy.

Similarly, the control agent acts on the system via a policy, also defined via parametric functions. The same adjoint-based framework is then used on the digital twin to identify the control policy and thus train the agent in the so-called “model-based” training. At the same time, a reinforcement learning approach using the Deep Deterministic Policy Gradient (DDPG) pursues the same task of training the control agent

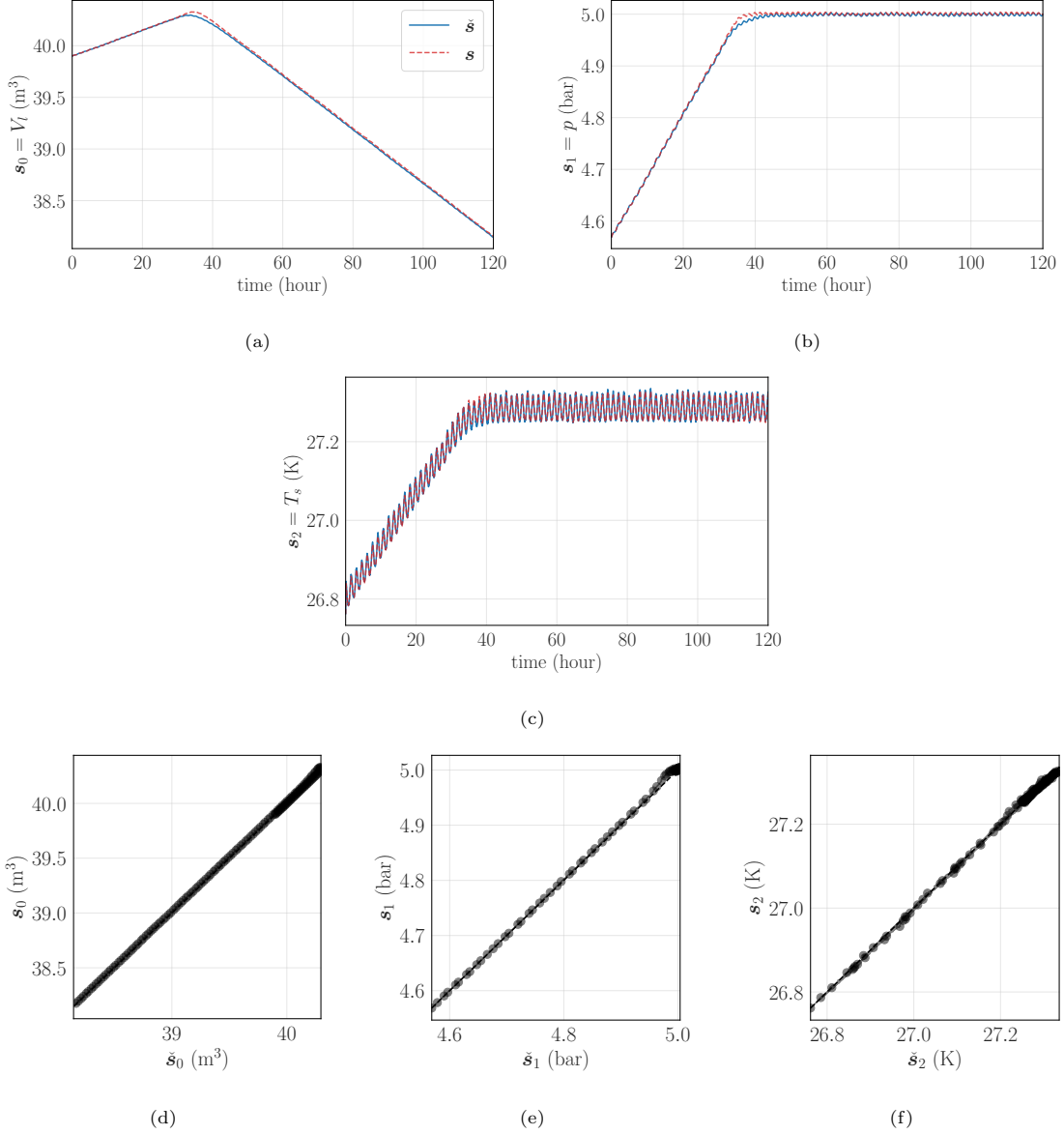


Figure 21: Performance of the digital twin assimilation. (a) Cost function \mathcal{L}_p normalized with its initial value $\mathcal{L}_p(\mathbf{w}_p^0)$ over the number of episodes. Agreement of the predicted state $\mathbf{s} = [V_i, p, T_s]$ with the real state $\tilde{\mathbf{s}}$ shown through (b) a scatter plot, and (c) the time series evolution.

without using explicit knowledge of the system in the so-called “model-free” training. The “model-based” and the “model-free” policies are then tested on the digital twin once this has reached satisfying predictive performances and the best-performing policy becomes the “live policy” taken on the real system. We explored a first mechanism to let both the “model-based” and the “model-free” learn from the live policy and showed that this can create a virtuous loop in which both approaches lead to a sequence of improvements over the other.

We tested this novel framework on three widely different engineering systems: a wind turbine in a time-varying wind speed, a flapping-wing micro air vehicle travelling against gusts, and the thermal management of a cryogenic tank subject to time-varying heat loads. In these problems, the physics-based model of the

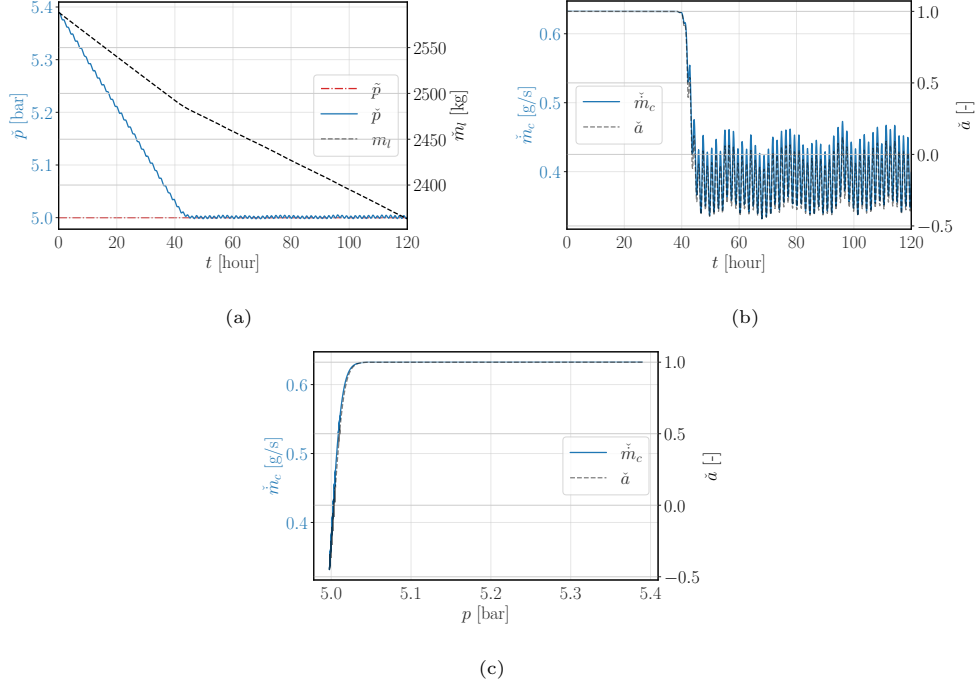


Figure 22: Tracking performance of the pressure \check{p} , and variation of propellant mass \check{m}_l over the real environment, starting from an over-pressure condition. Corresponding control action \check{a} and vented mass flow rate \check{m}_c . Thermodynamic actuation \check{m}_v and \check{a} as a function of the pressure p . The acting policy $\pi(\check{e}; \mathbf{w}_a)$ is retrieved by taking the optimal set of weights \mathbf{w}_a from the training.

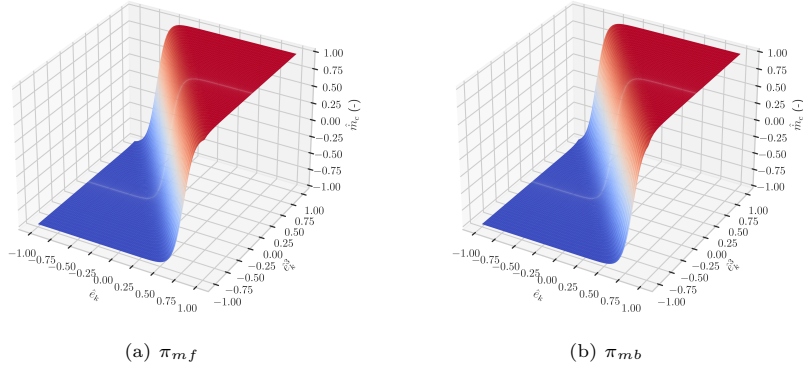


Figure 23: Surface plot of the found policies, π_{mf} (23a) and π_{mb} (23b).

digital twin is formulated as ODEs ensuring the compliance of predictions with fundamental principles (conservation of angular momentum in a wind turbine, Newton's law in the drone's trajectory and conservation of mass/energy within the cryogenic tank) and the closure law describe unmodelled physics (aerodynamic coefficients and heat transfer correlations).

The performance of the Reinforcement Twinning framework, both in training the digital twin and the controlling agent, proves the framework's potential beyond any specific application. The merit stems from the complementary characteristics of the two approaches, the model-based being extremely sample-efficient but prone to fall stuck into local minima and the model-free being sample-inefficient but able to explore the parameter space better.

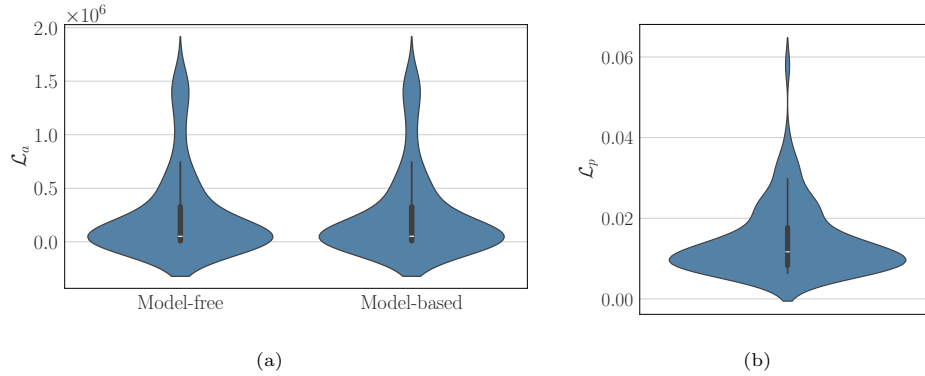


Figure 24: Violin plots obtained after 100 runs for the (a) assimilation performance and (b) model-based and model-free controllers.

The paths towards future extensions are many. On the one hand, we could introduce a more advanced learning feedback mechanism between the model-free and the model-based methods, which is currently limited to a “cloning” procedure. This could allow, for example, different policy architecture between the two, unleashing the potential of reinforcement learning to handle arbitrarily complex policies in the form of an artificial neural network. On the other hand, we could introduce more sophisticated methods of integrating the digital twin in the training of the model-free loop, for instance, by using the virtual environment to boost the training of the critic network with strategies akin to traditional model-based reinforcement learning.

Nevertheless, these preliminary results open the path towards further hybridization of model-based and model-free methods and, more broadly, between traditional engineering and machine learning. Such a combination is essential to profit from the ever-growing availability of real-time data to achieve excellent predictive and control capabilities without sacrificing interpretability.

References

- Tutorial overview of model predictive control. *IEEE Control Syst* 2000;20(3):38–52. URL: <https://ieeexplore.ieee.org/document/845037/>. doi:10.1109/37.845037.
- Abarbanel H, Rozdeba P, Shirman S. Machine learning, deepest learning: Statistical data assimilation problems. 2017. arXiv:1707.01415.
- Abbas NJ, Wright A, Pao L. An update to the national renewable energy laboratory baseline wind turbine controller. In: *Journal of Physics: Conference Series*. IOP Publishing; volume 1452; 2020. p. 012002.
- Ahmed SE, Pawar S, San O. PyDA: A hands-on introduction to dynamical data assimilation with python. *Fluids* 2020;5(4):225. doi:10.3390/fluids5040225.
- Ammar A, Nassereddine H, AbdulBaky N, AbouKansour A, Tannoury J, Urban H, Schranz C. Digital Twins in the Construction Industry: A Perspective of Practitioners and Building Authority. *Front Built Environ* 2022;8:834671. URL: <https://www.frontiersin.org/articles/10.3389/fbuil.2022.834671/full>. doi:10.3389/fbuil.2022.834671.
- Andersson C, Ribeiro AH, Tiels K, Wahlstrom N, Schon TB. Deep convolutional networks in system identification. In: 2019 IEEE 58th Conference on Decision and Control (CDC). IEEE; 2019. doi:10.1109/cdc40024.2019.9030219.
- Arcucci R, Zhu J, Hu S, Guo YK. Deep data assimilation: Integrating deep learning with data assimilation. *Applied Sciences* 2021;11(3):1114. doi:10.3390/app11031114.
- Asch M, Bocquet M, Nodet M. *Data Assimilation*. Society for Industrial and Applied Mathematics, 2016. doi:10.1137/1.9781611974546.
- Astrom KJ, Wittenmark B. *Adaptive Control*. 2nd ed. Prentice Hall, 1994.
- Ayed I, de Bézenac E, Pajot A, Brajard J, Gallinari P. Learning Dynamical Systems from Partial Observations. 2019. URL: <http://arxiv.org/abs/1902.11136>; arXiv:1902.11136 [physics].
- Baker N, Alexander F, Bremer T, Hagberg A, Kevrekidis Y, Najm H, Parashar M, Patra A, Sethian J, Wild S, Willcox K, Lee S. Workshop report on basic research needs for scientific machine learning: Core technologies for artificial intelligence 2019;URL: <https://www.osti.gov/biblio/1478744>. doi:10.2172/1478744.
- Barricelli BR, Casiraghi E, Fogli D. A survey on digital twin: Definitions, characteristics, applications, and design implications. *IEEE Access* 2019;7:167653–7. doi:10.1109/access.2019.2953499.
- Barsi S. Ventless Pressure Control of Cryogenic Storage Tanks. Ph.D. thesis; CASE Western Reserve University; 2011.
- Barsi S, Kassemi M. Investigation of tank pressurization and pressure control—part i: Experimental study. *Journal of Thermal Science and Engineering Applications* 2013a;5(4). doi:10.1115/1.4023891.
- Barsi S, Kassemi M. Investigation of tank pressurization and pressure control—part II: Numerical modeling. *Journal of Thermal Science and Engineering Applications* 2013b;5(4). doi:10.1115/1.4023892.
- van Beek A, Karkaria VN, Chen W. Digital twins for the designs of systems: a perspective. *Structural and Multidisciplinary Optimization* 2023;66(3). doi:10.1007/s00158-023-03488-x.
- Bertsekas D. *Reinforcement Learning and Optimal Control*. Athena Scientific, 2019.
- Bhatnagar S, Sutton RS, Ghavamzadeh M, Lee M. Natural actor–critic algorithms. *Automatica* 2009;45(11):2471–82. URL: <https://linkinghub.elsevier.com/retrieve/pii/S0005109809003549>. doi:10.1016/j.automatica.2009.07.008.
- Bhowmik S, Spee R. Performance Optimization for Doubly Fed Wind Power Generation Systems. *IEEE TRANSACTIONS ON INDUSTRY APPLICATIONS* 1999;35(4).
- Bianchi FD, De Battista H, Mantz RJ. *Wind turbine control systems: principles, modelling and gain scheduling design*. volume 19. Springer, 2007.
- Bocquet M. Ensemble kalman filtering without the intrinsic need for inflation. *Nonlinear Processes in Geophysics* 2011;18(5):735–50. doi:10.5194/npg-18-735-2011.
- Bocquet M, Brajard J, Carrassi A, Bertino L. Data assimilation as a deep learning tool to infer ode representations of dynamical models. 2019. .
- Bocquet M, Farchi A. Introduction to the principles and methods of data assimilation in the geosciences. Technical Report; École des Ponts ParisTech; 2023.
- Boedecker J, Springenberg JT, Wülfing J, Riedmiller M. Approximate real-time optimal control based on sparse gaussian process models. In: 2014 IEEE Symposium on Adaptive Dynamic Programming and Reinforcement Learning (ADPRL). 2014a. p. 1–8. doi:10.1109/ADPRL.2014.7010608.
- Boedecker J, Springenberg JT, Wülfing J, Riedmiller M. Approximate real-time optimal control based on sparse gaussian process models. In: 2014 IEEE Symposium on Adaptive Dynamic Programming and Reinforcement Learning (ADPRL). 2014b. p. 1–8. doi:10.1109/ADPRL.2014.7010608.
- Bossanyi EA. The Design of closed loop controllers for wind turbines. *Wind Energy* 2000;3(3):149–63. URL: <https://onlinelibrary.wiley.com/doi/10.1002/we.34>. doi:10.1002/we.34.
- Bradley AM. Pde-constrained optimization and the adjoint method 2019;.
- Brajard J, Carassi A, Bocquet M, Bertino L. Combining data assimilation and machine learning to emulate a dynamical model from sparse and noisy observations: a case study with the Lorenz 96 model. *Journal of Computational Science* 2020;44:101171. URL: <http://arxiv.org/abs/2001.01520>. doi:10.1016/j.jocs.2020.101171; arXiv:2001.01520 [physics, stat].
- Branlard E, Jonkman J, Brown C, Zang J. A digital-twin solution for floating offshore wind turbines validated using a full-scale prototype. *Wind Energy Science Discussions* 2023;2023:1–34. URL: <https://wes.copernicus.org/preprints/wes-2023-50/>. doi:10.5194/wes-2023-50.
- Buizza C, Casas CQ, Nadler P, Mack J, Marrone S, Titus Z, Cornec CL, Heylen E, Dur T, Ruiz LB, Heaney C, Lopez JAD,

- Kumar KS, Arcucci R. Data learning: Integrating data assimilation and machine learning. *Journal of Computational Science* 2022;58:101525. doi:10.1016/j.jocs.2021.101525.
- Cai X, Kolomenskiy D, Nakata T, Liu H. A cfd data-driven aerodynamic model for fast and precise prediction of flapping aerodynamics in various flight velocities. *Journal of Fluid Mechanics* 2021;915:A114.
- Canaday D, Pomerance A, Gauthier DJ. Model-free control of dynamical systems with deep reservoir computing. 2020. arXiv:2010.02285.
- Cao Y, Li S, Petzold L, Serban R. Adjoint sensitivity analysis for differential-algebraic equations: The adjoint DAE system and its numerical solution. *SIAM Journal on Scientific Computing* 2003;24(3):1076–89. doi:10.1137/s1064827501380630.
- Carrassi A, Bocquet M, Bertino L, Evensen G. Data assimilation in the geosciences - an overview on methods, issues and perspectives. 2017. arXiv:1709.02798.
- Cengel Y, Ghajar A. *Heat and Mass Transfer: Fundamentals and Applications*. 6th ed. McGraw Hill, 2019.
- Chai PR, Willhite AW. Cryogenic thermal system analysis for orbital propellant depot. 2014. URL: <https://linkinghub.elsevier.com/retrieve/pii/S0094576514001738>. doi:10.1016/j.actaastro.2014.05.013.
- Chang CC, Lin CJ. LIBSVM. *ACM Transactions on Intelligent Systems and Technology* 2011;2(3):1–27. doi:10.1145/1961189.1961199.
- Chatzilygeroudis K, Vassiliades V, Stulp F, Calinon S, Mouret JB. A survey on policy search algorithms for learning robot controllers in a handful of trials. 2019. arXiv:1807.02303.
- Chen RTQ, Rubanova Y, Bettencourt J, Duvenaud D. Neural ordinary differential equations. In: *Proceedings of the 32nd International Conference on Neural Information Processing Systems*. Red Hook, NY, USA: Curran Associates Inc.; NIPS'18; 2018. p. 6572–6583.
- Chen S, Billings S, Grant P. Non-linear system identification using neural networks. *International Journal of Control* 1990;51(6):1191–214. doi:10.1080/00207179008934126.
- Cheng B, Tobalske BW, Powers DR, Hedrick TL, Wethington SM, Chiu GT, Deng X. Flight mechanics and control of escape manoeuvres in hummingbirds. i. flight kinematics. *Journal of Experimental Biology* 2016;219(22):3518–31.
- Cheng S, Quilodran-Casas C, Oualla S, Farchi A, Liu C, Tandeo P, Fablet R, Lucor D, Iooss B, Brajard J, Xiao D, Janjic T, Ding W, Guo Y, Carrassi A, Bocquet M, Arcucci R. Machine learning with data assimilation and uncertainty quantification for dynamical systems: a review. 2023. URL: <http://arxiv.org/abs/2303.10462>; arXiv:2303.10462 [cs].
- Chinesta F, Cueto E, Abisset-Chavanne E, Duval JL, Khaldi FE. Virtual, Digital and Hybrid Twins: A New Paradigm in Data-Based Engineering and Engineered Data. *Arch Computat Methods Eng* 2020;27(1):105–34. URL: <http://link.springer.com/10.1007/s11831-018-9301-4>. doi:10.1007/s11831-018-9301-4.
- Deisenroth M, Rasmussen C. Pilco: A model-based and data-efficient approach to policy search. 2011. p. 465–72.
- Dickinson MH, Lehmann FO, Sane SP. Wing rotation and the aerodynamic basis of insect flight. *Science* 1999;284(5422):1954–60.
- Dimet FXL, Navon IM, Ștefănescu R. Variational data assimilation: Optimization and optimal control. In: *Data Assimilation for Atmospheric, Oceanic and Hydrologic Applications (Vol. III)*. Springer International Publishing; 2016. p. 1–53. doi:10.1007/978-3-319-43415-5_1.
- Errico RM. What is an adjoint model? *Bulletin of the American Meteorological Society* 1997;78(11).
- Evensen G. *Data Assimilation: The Ensemble Kalman Filter*. 2nd ed. Spinger, 2009.
- Fahim M, Sharma V, Cao TV, Canberk B, Duong TQ. Machine learning-based digital twin for predictive modeling in wind turbines. *IEEE Access* 2022;10:14184–94. URL: <https://api.semanticscholar.org/CorpusID:246420062>.
- Fei F, Tu Z, Yang Y, Zhang J, Deng X. Flappy hummingbird: An open source dynamic simulation of flapping wing robots and animals. In: *2019 International Conference on Robotics and Automation (ICRA)*. IEEE; 2019. p. 9223–9.
- Geer AJ. Learning earth system models from observations: machine learning or data assimilation? *Philosophical Transactions of the Royal Society A: Mathematical, Physical and Engineering Sciences* 2021;379(2194). doi:10.1098/rsta.2020.0089.
- Gonzalez J, Yu W. Non-linear system modeling using LSTM neural networks. *IFAC-PapersOnLine* 2018;51(13):485–9. doi:10.1016/j.ifacol.2018.07.326.
- Goodfellow I, Bengio Y, Courville A, Bengio Y. *Deep learning*. volume 1. MIT press Cambridge, 2016.
- Haarnoja T, Zhou A, Abbeel P, Levine S. Soft actor-critic: Off-policy maximum entropy deep reinforcement learning with a stochastic actor. 2018. arXiv:1801.01290.
- Haghshenas A, Hasan A, Osen O, Mikalsen ET. Predictive digital twin for offshore wind farms. *Energy Informatics* 2023;6(1):1–26.
- Haider N, Shahzad A, Qadri MNM, Shah SIA. Recent progress in flapping wings for micro aerial vehicle applications. *Proceedings of the Institution of Mechanical Engineers, Part C: Journal of Mechanical Engineering Science* 2020;235(2):245–64. doi:10.1177/0954406220917426.
- Hastings L, Tucker S, Flachbart R, Hedayat A, Nelson S. Marshall space flight center in-space cryogenic fluid management program overview. In: *41st AIAA/ASME/SAE/ASEE Joint Propulsion Conference and Exhibit*. American Institute of Aeronautics and Astronautics; 2005. doi:10.2514/6.2005-3561.
- Hastings LJ, Flachbart R, Martin J, Hedayat A, Fazah M, Lak T, Nguyen H, Bailey J. Spray Bar Zero-Gravity Vent System for On-Orbit Liquid Hydrogen Storage. *Technical Memorandum (TM) NASA/TM-2003-212926*; National Aeronautics and Space Administration, Marshall Space Flight Center; Alabama 35812; 2003. URL: <https://ntrs.nasa.gov/api/citations/20040000092/downloads/20040000092.pdf>.
- Hedengren JD, Shishavan RA, Powell KM, Edgar TF. Nonlinear modeling, estimation and predictive control in AP-Monitor. *Computers & Chemical Engineering* 2014;70:133–48. URL: <https://linkinghub.elsevier.com/retrieve/pii/S0098135414001306>. doi:10.1016/j.compchemeng.2014.04.013.
- Hochreiter S, Schmidhuber J. Long short-term memory. *Neural Computation* 1997;9(8):1735–80. doi:10.1162/neco.1997.9.

- 8.1735.
- Howlader AM, Urasaki N, Uchida K, Yona A, Senjyu T, Kim CH, Saber AY. Parameter Identification of Wind Turbine for Maximum Power-point Tracking Control. *Electric Power Components and Systems* 2010;38(5):603–14. URL: <http://www.tandfonline.com/doi/abs/10.1080/15325000903376974>. doi:10.1080/15325000903376974.
- Hunt K, Sbarbaro D, Żbikowski R, Gawthrop P. Neural networks for control systems—a survey. *Automatica* 1992;28(6):1083–112. URL: <https://www.sciencedirect.com/science/article/pii/000510989290053I>. doi:[https://doi.org/10.1016/0005-1098\(92\)90053-I](https://doi.org/10.1016/0005-1098(92)90053-I).
- Imai R, Nishida K, Kawanami O, Umemura Y, Himeno T. Ground based experiment and numerical calculation on thermodynamic vent system in propellant tank for future cryogenic propulsion system. *Cryogenics* 2020;109:103095. doi:10.1016/j.cryogenics.2020.103095.
- Jaeger H, Haas H. Harnessing nonlinearity: Predicting chaotic systems and saving energy in wireless communication. *Science* 2004;304(5667):78–80. doi:10.1126/science.1091277.
- Jiang W, Sun P, Li P, Zuo Z, Huang Y. Transient thermal behavior of multi-layer insulation coupled with vapor cooled shield used for liquid hydrogen storage tank. *Energy* 2021;231:120859. doi:10.1016/j.energy.2021.120859.
- Johnson KE. Adaptive torque control of variable speed wind turbines. University of Colorado at Boulder, 2004.
- Johnson KE. Control of variable-speed wind turbines: standard and adaptive techniques for maximizing energy capture. *IEEE Control Systems Magazine* 2006;26(3):70–81.
- Jonkman BJ. TurbSim user’s guide. Technical Report; National Renewable Energy Lab.(NREL), Golden, CO (United States); 2006.
- Jonkman J, Butterfield S, Musial W, Scott G. Definition of a 5-MW reference wind turbine for offshore system development. Technical Report; National Renewable Energy Lab.(NREL), Golden, CO (United States); 2009.
- Kalnay E, Li H, Miyoshi T, Yang SC, Ballabrera-Poy J. 4-d-var or ensemble kalman filter? *Tellus A: Dynamic Meteorology and Oceanography* 2007;59(5):758. doi:10.1111/j.1600-0870.2007.00261.x.
- Khandelwal P, Nadler P, Arcucci R, Knottenbelt W, Guo YK. A scalable inference method for large dynamic economic systems. 2021. [arXiv:2110.14346](https://arxiv.org/abs/2110.14346).
- Kruyt JW, Quicazán-Rubio EM, Van Heijst GF, Althshuler DL, Lentink D. Hummingbird wing efficacy depends on aspect ratio and compares with helicopter rotors. *Journal of the royal society interface* 2014;11(99):20140585.
- Kurutach T, Clavera I, Duan Y, Tamar A, Abbeel P. Model-ensemble trust-region policy optimization. [arXiv preprint arXiv:180210592](https://arxiv.org/abs/180210592) 2018;.
- Lahoz W, Khattatov B, Menard R, editors. *Data Assimilation*. Springer Berlin Heidelberg, 2010. doi:10.1007/978-3-540-74703-1.
- Laks JH, Pao LY, Wright AD. Control of wind turbines: Past, present, and future. In: 2009 American Control Conference. IEEE; 2009. doi:10.1109/acc.2009.5160590.
- LeCun Y, Boser B, Denker JS, Henderson D, Howard RE, Hubbard W, Jackel LD. Backpropagation applied to handwritten zip code recognition. *Neural Computation* 1989;1(4):541–51. doi:10.1162/neco.1989.1.4.541.
- Lee Y, Lua KB, Lim T, Yeo K. A quasi-steady aerodynamic model for flapping flight with improved adaptability. *Bioinspiration & biomimetics* 2016;11(3):036005.
- Leishman JG. Challenges in modelling the unsteady aerodynamics of wind turbines. *Wind Energy: An International Journal for Progress and Applications in Wind Power Conversion Technology* 2002;5(2-3):85–132.
- Lemmon EW, Bell IH, Huber ML, McLinden MO. NIST Standard Reference Database 23: Reference Fluid Thermodynamic and Transport Properties-REFPROP, Version 10.0, National Institute of Standards and Technology. 2018. URL: <https://www.nist.gov/srd/refprop>. doi:<https://doi.org/10.18434/T4/1502528>.
- Lillicrap TP, Hunt JJ, Pritzel A, Heess N, Erez T, Tassa Y, Silver D, Wierstra D. Continuous control with deep reinforcement learning. 2019. [arXiv:1509.02971](https://arxiv.org/abs/1509.02971).
- Lin C, Dresar N, Hasan M. Pressure control analysis of cryogenic storage systems. *Journal of Propulsion and Power* 1991;20. doi:10.2514/1.10387.
- Liu X, MacArt JF. Adjoint-based machine learning for active flow control. 2023. [arXiv:2307.09980](https://arxiv.org/abs/2307.09980).
- Liu XY, Wang JX. Physics-informed dyna-style model-based deep reinforcement learning for dynamic control. 2021. doi:10.1098/rspa.2021.0618. [arXiv:2108.00128](https://arxiv.org/abs/2108.00128).
- Ljung L. Perspectives on system identification. *IFAC Proceedings Volumes* 2008;41(2):7172–84. doi:10.3182/20080706-5-kr-1001.01215.
- Ljung L, Andersson CR, Tiels K, Schön TB. Deep learning and system identification. *IFAC-PapersOnLine* 2020;URL: <https://api.semanticscholar.org/CorpusID:226118683>.
- Lorenz AC. Analysis methods for numerical weather prediction. *Quarterly Journal of the Royal Meteorological Society* 1986;112(474):1177–94. doi:10.1002/qj.49711247414.
- Lorenz AC, Bowler NE, Clayton AM, Pring SR, Fairbairn D. Comparison of hybrid-4denvar and hybrid-4dvar data assimilation methods for global NWP. *Monthly Weather Review* 2015;143(1):212–29. doi:10.1175/mwr-d-14-00195.1.
- Luo FM, Xu T, Lai H, Chen XH, Zhang W, Yu Y. A survey on model-based reinforcement learning. 2022a. URL: <http://arxiv.org/abs/2206.09328>. doi:10.48550/arXiv.2206.09328. [arXiv:2206.09328](https://arxiv.org/abs/2206.09328) [cs].
- Luo FM, Xu T, Lai H, Chen XH, Zhang W, Yu Y. A survey on model-based reinforcement learning. 2022b. [arXiv:2206.09328](https://arxiv.org/abs/2206.09328).
- Lutter M, Ritter C, Peters J. Deep lagrangian networks: Using physics as model prior for deep learning. 2019. [arXiv:1907.04490](https://arxiv.org/abs/1907.04490).
- Lutter M, Silberbauer J, Watson J, Peters J. Differentiable physics models for real-world offline model-based reinforcement learning. 2020. [arXiv:2011.01734](https://arxiv.org/abs/2011.01734).
- Madhavan P. Recurrent neural network for time series prediction. In: *Proceedings of the 15th Annual International Conference*

- of the IEEE Engineering in Medicine and Biology Society. IEEE; 1993. doi:10.1109/iembs.1993.978527.
- Marques P, Ahizi S, Mendez MA. Real Time Data Assimilation for the Thermodynamic Modeling of a Cryogenic Fuel Tank. In: 36th International Conference on Efficiency, Cost, Optimization, Simulation and Environmental Impact of Energy Systems (ECOS 2023). Las Palmas De Gran Canaria, Spain: ECOS 2023; 2023. p. 1041–52. URL: <http://www.proceedings.com/069564-0095.html>. doi:10.52202/069564-0095.
- Mer S, Fernandez D, Thibault JP, Corre C. Optimal design of a thermodynamic vent system for cryogenic propellant storage. *Cryogenics* 2016a;80:127–37. doi:10.1016/j.cryogenics.2016.09.012.
- Mer S, Thibault JP, Corre C. Active insulation technique applied to the experimental analysis of a thermodynamic control system for cryogenic propellant storage. *Journal of Thermal Science and Engineering Applications* 2016b;8(2). doi:10.1115/1.4032761.
- Mnih V, Kavukcuoglu K, Silver D, Graves A, Antonoglou I, Wierstra D, Riedmiller M. Playing atari with deep reinforcement learning. 2013a. arXiv:1312.5602.
- Mnih V, Kavukcuoglu K, Silver D, Graves A, Antonoglou I, Wierstra D, Riedmiller M. Playing atari with deep reinforcement learning. 2013b. arXiv:<http://arxiv.org/abs/1312.5602v1>.
- Mnih V, Kavukcuoglu K, Silver D, Rusu AA, Veness J, Bellemare MG, Graves A, Riedmiller M, Fidjeland AK, Ostrovski G, Petersen S, Beattie C, Sadik A, Antonoglou I, King H, Kumaran D, Wierstra D, Legg S, Hassabis D. Human-level control through deep reinforcement learning. *Nature* 2015;518(7540):529–33. doi:10.1038/nature14236.
- Moerland TM, Broekens J, Plaat A, Jonker CM. Model-based reinforcement learning: A survey. 2022a. URL: <http://arxiv.org/abs/2006.16712>. doi:10.48550/arXiv.2006.16712. arXiv:2006.16712 [cs, stat].
- Moerland TM, Broekens J, Plaat A, Jonker CM. Model-based reinforcement learning: A survey. 2022b. arXiv:2006.16712.
- Moriarty PJ, Hansen AC. AeroDyn theory manual. Technical Report; National Renewable Energy Lab., Golden, CO (US); 2005.
- Motil S, Meyer M, Tucker S. Cryogenic fluid management technologies for advanced green propulsion systems. In: 45th AIAA Aerospace Sciences Meeting and Exhibit. American Institute of Aeronautics and Astronautics; 2007. doi:10.2514/6.2007-343.
- Nadler P, Arcucci R, Guo Y. A neural sir model for global forecasting. In: Alsentzer E, McDermott MBA, Falck F, Sarkar SK, Roy S, Hyland SL, editors. Proceedings of the Machine Learning for Health NeurIPS Workshop. PMLR; volume 136 of *Proceedings of Machine Learning Research*; 2020. p. 254–66. URL: <https://proceedings.mlr.press/v136/nadler20a.html>.
- Nagabandi A, Kahn G, Fearing RS, Levine S. Neural network dynamics for model-based deep reinforcement learning with model-free fine-tuning. 2017. arXiv:1708.02596.
- Nelles O. Nonlinear System Identification. Springer Berlin Heidelberg, 2001. doi:10.1007/978-3-662-04323-3.
- Nicolao GD. System identification : Problems and perspectives. In: 12th Workshop on Qualitative Reasoning. 2003. URL: <https://api.semanticscholar.org/CorpusID:26963940>.
- Norgaard M, Ravn O, Poulsen N, Hansen L. Neural Networks for Modelling and Control of Dynamic Systems. Advanced Textbooks in Control and Signal Processing. Springer London, 2000.
- Olatunji OO, Adedeji PA, Madushele N, Jen TC. Overview of digital twin technology in wind turbine fault diagnosis and condition monitoring. 2021 IEEE 12th International Conference on Mechanical and Intelligent Manufacturing Technologies (ICMIMT) 2021;:201–7URL: <https://api.semanticscholar.org/CorpusID:236190314>.
- Ortega-Jiménez VM, Dudley R. Ascending flight and decelerating vertical glides in anna’s hummingbirds. *Journal of Experimental Biology* 2018;221(24):jeb191171.
- Panzarella C, Plachta D, Kassemi M. Pressure control of large cryogenic tanks in microgravity. 2004. URL: <https://linkinghub.elsevier.com/retrieve/pii/S0011227504000633>. doi:10.1016/j.cryogenics.2004.03.009.
- Panzarella CH, Kassemi M. On the validity of purely thermodynamic descriptions of two-phase cryogenic fluid storage. 2003. URL: http://www.journals.cambridge.org/abstract_S0022112003004002. doi:10.1017/S0022112003004002.
- Pao LY, Johnson KE. A tutorial on the dynamics and control of wind turbines and wind farms. In: 2009 American Control Conference. IEEE; 2009. doi:10.1109/acc.2009.5160195.
- Pillonetto G, Aravkin A, Gedon D, Ljung L, Ribeiro AH, Schön TB. Deep networks for system identification: a survey. 2023. arXiv:2301.12832.
- Pimenta F, Pacheco J, Branco CM, Teixeira CM, Magalhães F. Development of a digital twin of an onshore wind turbine using monitoring data. *Journal of Physics: Conference Series* 2020;1618(2):022065. URL: <https://dx.doi.org/10.1088/1742-6596/1618/2/022065>. doi:10.1088/1742-6596/1618/2/022065.
- Pino F, Schena L, Rabault J, Mendez MA. Comparative analysis of machine learning methods for active flow control. *Journal of Fluid Mechanics* 2023;958. doi:10.1017/jfm.2023.76.
- Pu Z, Kalnay E. Numerical weather prediction basics: Models, numerical methods, and data assimilation. In: Handbook of Hydrometeorological Ensemble Forecasting. Springer Berlin Heidelberg; 2018. p. 1–31. doi:10.1007/978-3-642-40457-3_11-1.
- Puterman ML. Markov Decision Processes. Wiley, 1994. doi:10.1002/9780470316887.
- Qin X, Li P, Sun P, Huang Y. Testing and comparison of a thermodynamic vent system operating in different modes in a liquid nitrogen tank. *Applied Thermal Engineering* 2021;197:117393. doi:10.1016/j.applthermaleng.2021.117393.
- Rahman A, Drgoña J, Tuor A, Strube J. Neural ordinary differential equations for nonlinear system identification. 2022. arXiv:2203.00120.
- Raissi M, Perdikaris P, Karniadakis GE. Physics-informed neural networks: A deep learning framework for solving forward and inverse problems involving nonlinear partial differential equations. *Journal of Computational physics* 2019;378:686–707.
- Ramesh A, Ravindran B. Physics-informed model-based reinforcement learning. 2023. arXiv:2212.02179.
- Rasheed A, San O, Kvamsdal T. Digital Twin: Values, Challenges and Enablers. 2019. URL: <http://arxiv.org/abs/1910>.

- 01719; arXiv:1910.01719 [eess].
- Rasmussen CE, Williams CKI. Gaussian Processes for Machine Learning. MIT Press Ltd, 2005.
- Routray A, Osuri KK, Pattanayak S, Mohanty UC. Introduction to data assimilation techniques and ensemble kalman filter. In: Advanced Numerical Modeling and Data Assimilation Techniques for Tropical Cyclone Prediction. Springer Netherlands; 2016. p. 307–30. doi:10.5822/978-94-024-0896-6_11.
- Saint-Drenan YM, Besseau R, Jansen M, Staffell I, Troccoli A, Dubus L, Schmidt J, Gruber K, Simões SG, Heier S. A parametric model for wind turbine power curves incorporating environmental conditions. Renewable Energy 2020;157:754–68. URL: <https://www.sciencedirect.com/science/article/pii/S0960148120306613>. doi:<https://doi.org/10.1016/j.renene.2020.04.123>.
- Salzman JA. Fluid management in space-based systems. In: Engineering, Construction, and Operations in Space V. American Society of Civil Engineers; 1996. doi:10.1061/40177(207)71.
- Sane SP. The aerodynamics of insect flight. Journal of experimental biology 2003;206(23):4191–208.
- Sane SP, Dickinson MH. The control of flight force by a flapping wing: lift and drag production. Journal of experimental biology 2001;204(15):2607–26.
- Sastry SS, Isidori A. Adaptive control of linearizable systems. IEEE Transactions on Automatic Control 1989;34(11):1123–31.
- Schaul T, Quan J, Antonoglou I, Silver D. Prioritized experience replay. 2015. doi:10.48550/ARXIV.1511.05952.
- Schaul T, Quan J, Antonoglou I, Silver D. Prioritized experience replay. 2016. arXiv:1511.05952.
- Schoukens J, Ljung L. Nonlinear system identification: A user-oriented road map. IEEE Control Systems 2019;39(6):28–99. doi:10.1109/mcs.2019.2938121.
- Schwenzer M, Ay M, Bergs T, Abel D. Review on model predictive control: an engineering perspective. Int J Adv Manuf Technol 2021;117(5-6):1327–49. URL: <https://link.springer.com/10.1007/s00170-021-07682-3>. doi:10.1007/s00170-021-07682-3.
- Silver D, Huang A, Maddison CJ, Guez A, Sifre L, van den Driessche G, Schrittwieser J, Antonoglou I, Panneershelvam V, Lanctot M, Dieleman S, Grewe D, Nham J, Kalchbrenner N, Sutskever I, Lillicrap T, Leach M, Kavukcuoglu K, Graepel T, Hassabis D. Mastering the game of go with deep neural networks and tree search. Nature 2016;529(7587):484–9.
- Silver D, Hubert T, Schrittwieser J, Antonoglou I, Lai M, Guez A, Lanctot M, Sifre L, Kumaran D, Graepel T, Lillicrap T, Simonyan K, Hassabis D. A general reinforcement learning algorithm that masters chess, shogi, and go through self-play. Science 2018;362(6419):1140–4.
- Silver D, Lever G, Heess N, Degris T, Wierstra D, Riedmiller M. Deterministic Policy Gradient Algorithms 2014;.
- Sjöberg J, Hjalmarsson H, Ljung L. Neural networks in system identification. IFAC Proceedings Volumes 1994;27(8):359–82. doi:10.1016/s1474-6670(17)47737-8.
- Smola AJ, Schölkopf B. A tutorial on support vector regression. Statistics and Computing 2004;14(3):199–222. doi:10.1023/b:stco.0000035301.49549.88.
- Staffell I, Green R. How does wind farm performance decline with age? Renewable Energy 2014;66:775–86. URL: <https://www.sciencedirect.com/science/article/pii/S0960148113005727>. doi:<https://doi.org/10.1016/j.renene.2013.10.041>.
- Stengel RF. Optimal control and estimation. Courier Corporation, 1994.
- Sutton RS. Dyna, an integrated architecture for learning, planning, and reacting. SIGART Bull 1991;2(4):160–163. URL: <https://doi.org/10.1145/122344.122377>. doi:10.1145/122344.122377.
- Sutton RS, Barto AG. Reinforcement learning: An introduction. MIT press, 2018.
- Suykens JAK, Vandewalle JPL, Moor BLRD. Artificial Neural Networks for Modelling and Control of Non-Linear Systems. Springer US, 1996. doi:10.1007/978-1-4757-2493-6.
- Szita I. Reinforcement learning in games. In: Adaptation, Learning, and Optimization. Springer Berlin Heidelberg; 2012. p. 539–77.
- Taha HE, Hajj MR, Nayfeh AH. Flight dynamics and control of flapping-wing mavs: a review. Nonlinear Dynamics 2012;70:907–39.
- Talagrand O, Courtier P. Variational assimilation of meteorological observations with the adjoint vorticity equation. i: Theory. Quarterly Journal of the Royal Meteorological Society 1987;113(478):1311–28. doi:10.1002/qj.49711347812.
- Tang Y, Hsieh WW. Coupling neural networks to incomplete dynamical systems via variational data assimilation. Monthly Weather Review 2001;129(4):818–34. doi:10.1175/1520-0493(2001)129<0818:cnntid>2.0.co;2.
- Tekinerdogan B. On the notion of digital twins: A modeling perspective. 2022. URL: <https://www.mdpi.com/2079-8954/11/1/15>. doi:10.3390/systems11010015.
- Uc-Cetina V, Navarro-Guerrero N, Martin-Gonzalez A, Weber C, Wermter S. Survey on reinforcement learning for language processing. Artificial Intelligence Review 2022;56(2):1543–75. doi:10.1007/s10462-022-10205-5.
- Wagner R, Schleich B, Haefner B, Kuhnle A, Wartzack S, Lanza G. Challenges and potentials of digital twins and industry 4.0 in product design and production for high performance products. Procedia CIRP 2019;84:88–93. doi:10.1016/j.procir.2019.04.219.
- Wang B, Huang Y, Wu J, Wang T, Lei G. Experimental study on pressure control of liquid nitrogen tank by thermodynamic vent system. Applied Thermal Engineering 2017;125:1037–46. URL: <https://www.sciencedirect.com/science/article/pii/S1359431117315491>. doi:<https://doi.org/10.1016/j.applthermaleng.2017.07.067>.
- Wang B, Zou X, Zhu J. Data assimilation and its applications. Proceedings of the National Academy of Sciences 2000;97(21):11143–4. doi:10.1073/pnas.97.21.11143.
- Weber T, Racanière S, Reichert DP, Buesing L, Guez A, Rezende DJ, Badia AP, Vinyals O, Heess N, Li Y, Pascanu R, Battaglia P, Hassabis D, Silver D, Wierstra D. Imagination-augmented agents for deep reinforcement learning. 2017. arXiv:1707.06203.
- Werner S, Peitz S. Learning a model is paramount for sample efficiency in reinforcement learning control of pdes. 2023.

- arXiv:2302.07160.
- Whitney JP, Wood RJ. Aeromechanics of passive rotation in flapping flight. *Journal of fluid mechanics* 2010;660:197–220.
- Willard J, Jia X, Xu S, Steinbach M, Kumar V. Integrating scientific knowledge with machine learning for engineering and environmental systems. 2020. doi:10.48550/ARXIV.2003.04919.
- Wright L, Davidson S. How to tell the difference between a model and a digital twin. *Advanced Modeling and Simulation in Engineering Sciences* 2020;7(1). doi:10.1186/s40323-020-00147-4.
- Xue Y, Cai X, Xu R, Liu H. Wing kinematics-based flight control strategy in insect-inspired flight systems: Deep reinforcement learning gives solutions and inspires controller design in flapping mavs. *Biomimetics* 2023;8(3):295.
- Zhang C, Moore KL. System identification using neural networks. [1991] *Proceedings of the 30th IEEE Conference on Decision and Control* 1991;:873–874 vol.1URL: <https://api.semanticscholar.org/CorpusID:60798054>.
- Zhang H, Constantinescu EM. Optimal checkpointing for adjoint multistage time-stepping schemes. *Journal of Computational Science* 2023;66:101913. doi:10.1016/j.jocs.2022.101913.
- Zheng X, Jin T. A reliable method of wind power fluctuation smoothing strategy based on multidimensional non-linear exponential smoothing short-term forecasting. *IET Renewable Power Generation* 2022;16(16):3573–86. doi:10.1049/rpg2.12395.